



# Arctic Ocean CO<sub>2</sub> uptake: an improved multiyear estimate of the air–sea CO<sub>2</sub> flux incorporating chlorophyll *a* concentrations

Sayaka Yasunaka<sup>1,2</sup>, Eko Siswanto<sup>1</sup>, Are Olsen<sup>3</sup>, Mario Hoppema<sup>4</sup>, Eiji Watanabe<sup>2</sup>, Agneta Fransson<sup>5</sup>,  
Melissa Chierici<sup>6</sup>, Akihiko Murata<sup>1,2</sup>, Siv K. Lauvset<sup>3,7</sup>, Rik Wanninkhof<sup>8</sup>, Taro Takahashi<sup>9</sup>, Naohiro Kosugi<sup>10</sup>,  
Abdirahman M. Omar<sup>7</sup>, Steven van Heuven<sup>11</sup>, and Jeremy T. Mathis<sup>12</sup>

<sup>1</sup>Research and Development Center for Global Change, Japan Agency for Marine–Earth Science and Technology, Yokosuka, Japan

<sup>2</sup>Institute of Arctic Climate and Environment Research, Japan Agency for Marine–Earth Science and Technology, Yokosuka, Japan

<sup>3</sup>Geophysical Institute, University of Bergen and Bjerknes Centre for Climate Research, Bergen, Norway

<sup>4</sup>Alfred Wegener Institute Helmholtz Centre for Polar and Marine Research, Climate Sciences Department, Bremerhaven, Germany

<sup>5</sup>Norwegian Polar Institute, Fram Centre, Norway

<sup>6</sup>Institute of Marine Research, Tromsø, Norway

<sup>7</sup>Uni Research Climate, Bjerknes Centre for Climate Research, Bergen, Norway

<sup>8</sup>National Oceanic and Atmospheric Administration, Atlantic Oceanographic and Meteorological Laboratory, Miami, FL, USA

<sup>9</sup>Lamont–Doherty Earth Observatory of Columbia University, Palisades, NY, USA

<sup>10</sup>Oceanography and Geochemistry Research Department, Meteorological Research Institute, Japan Meteorological Agency, Tsukuba, Japan

<sup>11</sup>Energy and Sustainability Research Institute Groningen, Groningen University, the Netherlands

<sup>12</sup>National Oceanic and Atmospheric Administration, Arctic Research Program, Seattle, WA, USA

**Correspondence:** Sayaka Yasunaka (yasunaka@jamstec.go.jp)

Received: 25 July 2017 – Discussion started: 31 July 2017

Revised: 19 December 2017 – Accepted: 25 January 2018 – Published: 22 March 2018

**Abstract.** We estimated monthly air–sea CO<sub>2</sub> fluxes in the Arctic Ocean and its adjacent seas north of 60° N from 1997 to 2014. This was done by mapping partial pressure of CO<sub>2</sub> in the surface water ( $p\text{CO}_{2\text{w}}$ ) using a self-organizing map (SOM) technique incorporating chlorophyll *a* concentration (Chl *a*), sea surface temperature, sea surface salinity, sea ice concentration, atmospheric CO<sub>2</sub> mixing ratio, and geographical position. We applied new algorithms for extracting Chl *a* from satellite remote sensing reflectance with close examination of uncertainty of the obtained Chl *a* values. The overall relationship between  $p\text{CO}_{2\text{w}}$  and Chl *a* was negative, whereas the relationship varied among seasons and regions. The addition of Chl *a* as a parameter in the SOM process enabled us to improve the estimate of  $p\text{CO}_{2\text{w}}$ , particularly via better representation of its decline in spring, which re-

sulted from biologically mediated  $p\text{CO}_{2\text{w}}$  reduction. As a result of the inclusion of Chl *a*, the uncertainty in the CO<sub>2</sub> flux estimate was reduced, with a net annual Arctic Ocean CO<sub>2</sub> uptake of  $180 \pm 130 \text{ Tg C yr}^{-1}$ . Seasonal to interannual variation in the CO<sub>2</sub> influx was also calculated.

## 1 Introduction

The Arctic Ocean and its adjacent seas (Fig. 1) generally act as a sink for atmospheric CO<sub>2</sub> because of the high solubility of CO<sub>2</sub> in their low-temperature waters, combined with extensive primary production during the summer season (Bates and Mathis, 2009). The Arctic Ocean and its adjacent seas consist of complicated subregions that include continental

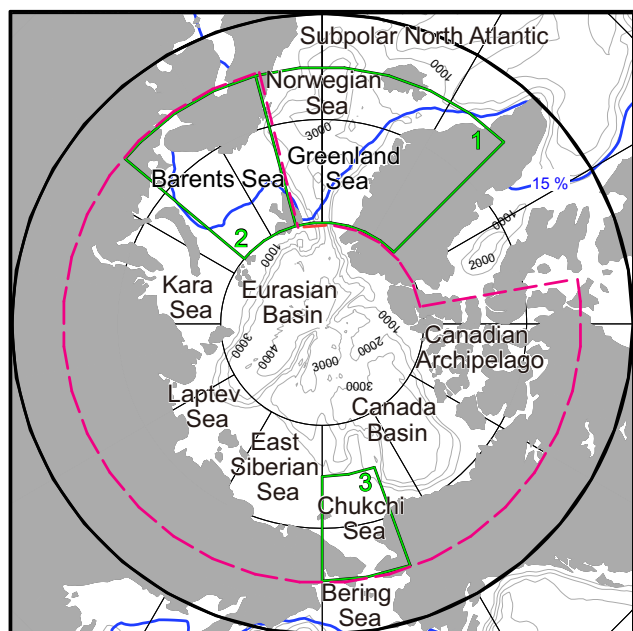


**Figure 1.** Map of the Arctic Ocean and its adjacent seas. Gray contour lines show the 1000, 2000, 3000, and 4000 m isobaths. Blue lines show the 17-year annual mean position of the ice edge (SIC = 15 %). Area for the mapping is north of 60° N (heavy black circle). Sectors selected for regional analysis are the Arctic Ocean (dashed magenta line), the Greenland and Norwegian seas (green 1), the Barents Sea (green 2), and the Chukchi Sea (green 3).

shelves, central basins, and sea-ice-covered areas. Therefore, the surface partial pressure of CO<sub>2</sub> ( $p\text{CO}_{2w}$ ) distribution is not only affected by ocean heat loss and gain, and biological production and respiration, but also by sea ice formation and melting, river discharge, and shelf–basin interactions (see Bates and Mathis, 2009, and references therein). However, CO<sub>2</sub> measurements are sparse in this very heterogeneous area (Fig. 2), and hence the existing air–sea CO<sub>2</sub> flux estimates in the Arctic are poorly constrained (Bates and Mathis, 2009; Schuster et al., 2013; Yasunaka et al., 2016).

As global warming progresses, melting of sea ice will increase the area of open water and enhance the potential for atmospheric CO<sub>2</sub> uptake (e.g., Bates et al., 2006; Gao et al., 2012). However, other processes could suppress CO<sub>2</sub> uptake. For example, increasing seawater temperatures, declining buffer capacity due to the freshening of Arctic surface water by increased river runoff and melting of sea ice, and increased vertical mixing supplying high-CO<sub>2</sub> water to the surface will all result in a tendency for reduced uptake (Bates and Mathis, 2009; Cai et al., 2010; Chierici et al., 2011; Else et al., 2013; Bates et al., 2014; Fransson et al., 2017). The combined effect of all these processes on ocean CO<sub>2</sub> uptake has not yet been clarified for the Arctic.

Yasunaka et al. (2016) prepared monthly maps of air–sea CO<sub>2</sub> fluxes from 1997 to 2013 for the Arctic north of 60° N by applying, for the first time, a self-organizing map (SOM)

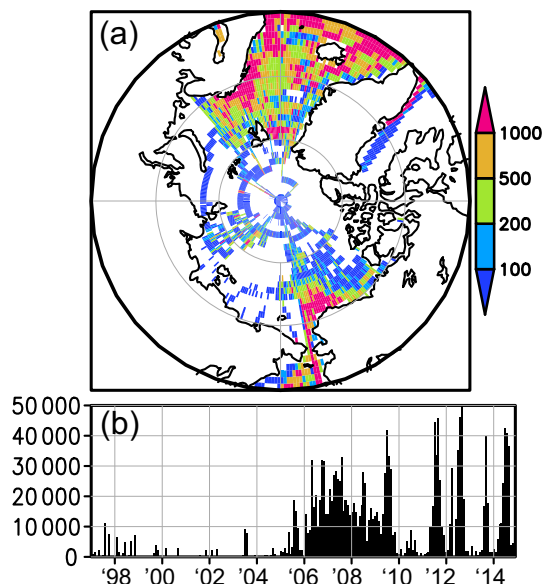


**Figure 2.** (a) The number of ocean surface CO<sub>2</sub> data in the grid boxes (1° × 1°) used in this study. Data are from SOCATv4, LDEOv2014, and GLODAPv2 and those collected by R/V *Mirai* of JAMSTEC between 1997 and 2014. (b) Monthly number of CO<sub>2</sub> data in the analysis area (north of 60° N) from 1997 to 2014.

technique to map  $p\text{CO}_{2w}$  in the Arctic Ocean. The advantage of the SOM technique is its ability to empirically determine relationships among variables without making any a priori assumptions (about what types of regression functions are applicable, and for which subregions the same regression function can be adopted, for example). The SOM technique has been shown to reproduce the distribution of  $p\text{CO}_{2w}$  from unevenly distributed observations better than multiple regression methods (Lefèvre et al., 2005; Telszewski et al., 2009). The uncertainty of the CO<sub>2</sub> flux estimated by Yasunaka et al. (2016), however, was large ( $\pm 3.4\text{--}4.6 \text{ mmol m}^{-2} \text{ d}^{-1}$ ), and the estimated CO<sub>2</sub> uptake in the Arctic Ocean was smaller than the uncertainty ( $180 \pm 210 \text{ Tg Cy}^{-1}$ ). One possible reason for the large uncertainties is that no direct proxies for the effect of biological processes on  $p\text{CO}_{2w}$  were used in that study, leading to an underestimation of the seasonal amplitude of  $p\text{CO}_{2w}$ .

Remotely sensed chlorophyll *a* concentrations (Chl *a*) have been used in several  $p\text{CO}_{2w}$  mapping efforts as a direct proxy for the effect of primary production. For example Chierici et al. (2009) produced  $p\text{CO}_{2w}$  algorithms for the subpolar North Atlantic during the period from May to October and found that the inclusion of Chl *a* improved the fit substantially. Measurements in several areas of the Arctic show that relationships between  $p\text{CO}_{2w}$  and Chl *a* also occur in this region. They correlate negatively (Gao et al., 2012; Ulfso et al., 2014), as expected from the drawdown of CO<sub>2</sub> during photosynthesis, but exceptions do occur; in coastal regions the correlation is positive (Mucci et al., 2010).

Several studies have demonstrated that Chl *a* in the Arctic can be estimated from satellite remote sensing reflectance (Rrs) (e.g., Arrigo and van Dijken, 2004; Cota et al., 2004). Perrette et al. (2011) showed that satellite-derived Chl *a* successfully captured a phytoplankton bloom in the ice edge region. Changes in the seasonal cycle from a single peak to a double peak of Chl *a* have also been detected and are likely a consequence of the recent sea ice loss in the Arctic (Ardyna et al., 2014). However, the available products (e.g., NASA's OceanColor dataset) in the Arctic include large uncertainty and many missing values because of sea ice, low angle of sunlight and cloud cover, and are also prone to error due to the co-occurrence of high colored dissolved organic matter (CDOM) and total suspended matter (TSM) concentrations (e.g., Matsuoka et al., 2007; Lewis et al., 2016). Here we deal with these issues by using several Chl *a* algorithms optimized for the Arctic and others, and by excluding Chl *a* data from grid cells potentially affected by CDOM and TSM. Calculated Chl *a* values were then interpolated so as to fit with the original data. Using these data, we examined the relationship between  $p\text{CO}_{2\text{w}}$  and Chl *a* in the Arctic Ocean and its adjacent seas and computed monthly air–sea CO<sub>2</sub> flux maps for regions north of 60° N using a SOM technique similar to that of Yasunaka et al. (2016) and with Chl *a* added to the SOM process.

## 2 Data

### 2.1 $p\text{CO}_{2\text{w}}$ measurements

We used fugacity of CO<sub>2</sub> ( $f\text{CO}_{2\text{w}}$ ) observations from the Surface Ocean CO<sub>2</sub> Atlas version 4 (SOCATv4; Bakker et al., 2016; <http://www.socat.info/>; 1 983 799 data points from > 60° N), and  $p\text{CO}_{2\text{w}}$  observations from the Global Surface  $p\text{CO}_2$  Database version 2014 (LDEOv2014; Takahashi et al., 2015; [http://cdiac.ornl.gov/oceans/LDEO\\_Underway\\_Database/](http://cdiac.ornl.gov/oceans/LDEO_Underway_Database/); 302 150 data points from > 60° N). In the LDEO database,  $p\text{CO}_{2\text{w}}$  is based on measured CO<sub>2</sub> mixing ratio in a parcel of air equilibrated with a seawater sample and computed assuming CO<sub>2</sub> as an ideal gas, whereas in the SOCAT,  $f\text{CO}_2$  is obtained considering the non-ideality from CO<sub>2</sub>–CO<sub>2</sub> and CO<sub>2</sub>–H<sub>2</sub>O molecular interactions. Because of ambiguities in the CO<sub>2</sub>–H<sub>2</sub>O interaction corrections, the SOCAT  $f\text{CO}_{2\text{w}}$  values are converted to  $p\text{CO}_{2\text{w}}$  values (a correction of < 1 %) and then combined with the LDEO  $p\text{CO}_{2\text{w}}$  values. When data points were duplicated in the SOCAT and LDEO datasets, the SOCAT version was used, except for the data obtained from onboard the USCGC *Healy* as these have been reanalyzed by Takahashi et al. (2015). Altogether 200 409 duplicates were removed. We also used shipboard  $p\text{CO}_{2\text{w}}$  data obtained during cruises of the R/V *Mirai* of the Japan Agency for Marine–Earth Science and Technology (JAMSTEC) that have not yet been included in SOCATv4 or LDEOv2014 (cruises MR09\_03, MR10\_05, MR12\_E03,

and MR13\_06; available at <http://www.godac.jamstec.go.jp/darwin/e/>; 95 725 data points from > 60° N). In total, we used 2 181 265  $p\text{CO}_{2\text{w}}$  data points, 33 % more than used by Yasunaka et al. (2016).

To further improve the data coverage, especially for the ice-covered regions, we also used 2166  $p\text{CO}_{2\text{w}}$  values calculated from dissolved inorganic carbon (DIC) and total alkalinity (TA) data extracted from the Global Ocean Data Analysis Project version 2 (GLODAPv2; Key et al., 2015; Olsen et al., 2016; <http://www.glodap.info/>). Of these data, 90 % were obtained at cruises without underway  $p\text{CO}_{2\text{w}}$  data. We extracted values of samples obtained from water depths shallower than 10 m, or the shallowest values from the upper 30 m of each cast if there were no values from above 10 m. There are 1795 data points above 10 m depth, 296 in the 10–20 m range, and 75 in the 20–30 m range. This resulted in 94 % more calculated  $p\text{CO}_{2\text{w}}$  values than used by Yasunaka et al. (2016), and altogether the number of directly measured and calculated data points used here is 33 % more than used in Yasunaka et al. (2016). The CO<sub>2</sub>SYS program (Lewis and Wallace, 1998; van Heuven et al., 2009) was used for the calculation with the dissociation constants reported by Lueker et al. (2000) and Dickson (1990).

We checked the difference between calculated  $p\text{CO}_{2\text{w}}$  and measured  $p\text{CO}_{2\text{w}}$  using the data from cruises with both bottle DIC and TA samples and underway  $p\text{CO}_{2\text{w}}$  available (10 % of the bottle samples, i.e., 245 pairs). The mean value for the calculated  $p\text{CO}_{2\text{w}}$  values from bottle DIC and TA samples from the upper 30 m was  $299 \pm 42 \mu\text{atm}$ , and that for the corresponding directly measured  $p\text{CO}_{2\text{w}}$  values from underway observation generally at 4–6 m was  $289 \pm 11 \mu\text{atm}$ . The mean values are slightly higher for calculated  $p\text{CO}_{2\text{w}}$  values than for measured ones, but the difference is smaller than the standard deviation and the uncertainties of the calculation (the latter of which is  $14 \mu\text{atm}$ ; see Sect. 4.2). The difference between calculated and measured  $p\text{CO}_{2\text{w}}$  is not dependent on the depth at which the TA and DIC samples were obtained. It was  $10 \pm 31 \mu\text{atm}$  for samples from above 10 m,  $7 \pm 27 \mu\text{atm}$  for samples from 10–20 m, and  $11 \pm 47 \mu\text{atm}$  for samples from 20 to 30 m.

The availability of  $p\text{CO}_{2\text{w}}$  data (measured and calculated) varies spatially and temporally (Fig. 2). Most of the available data are from the subpolar North Atlantic, the Greenland Sea, the Norwegian Sea, the Barents Sea, and the Chukchi Sea while much less data are available for the Kara Sea, the Laptev Sea, the East Siberian Sea, and the Eurasian Basin. The number of  $p\text{CO}_{2\text{w}}$  data increased after 2005, but there are also a substantial number of data from before 2004.

### 2.2 Other data

To calculate Chl *a*, we used merged Rrs data from the SeaWiFS, MODIS-Aqua, MERIS, and VIIRS ocean color sensors processed and distributed by the GlobColour Project (Mantorena et al., 2010; <http://hermes.acri.fr/index.php?class=>

archive). For compatibility with the spatiotemporal resolution of the gridded  $p\text{CO}_{2w}$  data (see below Sect. 3.3), we selected monthly mean Rrs data with a spatial resolution of  $1^\circ$  (latitude)  $\times$   $1^\circ$  (longitude).

Sea surface temperature (SST) data were extracted from the NOAA Optimum Interpolation SST Version 2 (Reynolds et al., 2002; <http://www.esrl.noaa.gov/psd/data/gridded/data.noaa.oisst.v2.html>). These data are provided at a resolution of  $1^\circ \times 1^\circ \times 1$  month. Sea surface salinity (SSS) data were retrieved from the Polar Science Center Hydrographic Climatology version 3.0, which also has a resolution of  $1^\circ \times 1^\circ \times 1$  month (Steele et al., 2001; [http://psc.apl.washington.edu/nonwp\\_projects/PHC/Climatology.html](http://psc.apl.washington.edu/nonwp_projects/PHC/Climatology.html)). Sea ice concentration (SIC) data were obtained from the NOAA National Snow and Ice Data Center Climate Data Record of Passive Microwave Sea Ice Concentration version 2, which has a resolution of  $25 \text{ km} \times 25 \text{ km} \times 1$  month (Meier et al., 2013; <http://nsidc.org/data/G02202>). These data were averaged into  $1^\circ \times 1^\circ \times 1$  month grid cells. Zonal mean data for the atmospheric CO<sub>2</sub> mixing ratio ( $x\text{CO}_{2a}$ ) were retrieved from the NOAA Greenhouse Gas Marine Boundary Layer Reference data product (Conway et al., 1994; <http://www.esrl.noaa.gov/gmd/ccgg/mbll/index.html>) and were interpolated into  $1^\circ \times 1^\circ \times 1$  month grid cells. Both sea level pressure and 6-hourly 10 m wind speed data were obtained from the US National Centers for Environmental Prediction–Department of Energy Reanalysis 2 (NCEP2) (Kanamitsu et al., 2002; <http://www.esrl.noaa.gov/psd/data/gridded/data.ncep.reanalysis2.html>). We also used the 6-hourly 10 m wind speeds from the US National Centers for Atmospheric Prediction and the National Center for Atmospheric Research Reanalysis 1 (NCEP1) (Kalnay et al., 1996; <https://www.esrl.noaa.gov/psd/data/gridded/data.ncep.reanalysis.html>) when the gas transfer velocity was optimized for NCEP2 wind (see Sect. 3.5 below).

Surface nitrate measurements were extracted from GLODAPv2 (Key et al., 2015; Olsen et al., 2016) and the World Ocean Database 2013 (WOD; Boyer et al., 2013). When data points were duplicated in the GLODAPv2 and WOD datasets, the GLODAPv2 version was used as this has been subjected to more extensive quality control.

### 3 Methods

#### 3.1 Calculation of chlorophyll *a* concentrations

Chl *a* was calculated from Rrs by using the Arctic algorithm developed by Cota et al. (2004). Several assessments have shown that this algorithm has a large uncertainty (e.g., Mat-suoka et al., 2007; Lewis et al., 2016), and therefore the sensitivity of our results to this choice was evaluated by using two alternative algorithms for Chl *a*: the standard algorithm

of O'Reilly et al. (1998) and the coastal algorithm of Tassan (1994).

To ensure that we were working with Rrs data relatively unaffected by CDOM and TSM, the Chl *a* data were masked following the method of Siswanto et al. (2013). Briefly, the Rrs spectral slope between 412 and 555 nm ( $\text{Rrs}_{555-412 \text{ slope}}$ ;  $\text{sr}^{-1} \text{ nm}^{-1}$ ) was plotted against logarithmically transformed Chl *a*. Based on the scatter plot of  $\log(\text{Chl } a)$  and  $\text{Rrs}_{555-412 \text{ slope}}$ , we then defined a boundary line separating phytoplankton-dominated grid cells ( $\text{Rrs}_{555-412 \text{ slope}} < \text{boundary value}$ ) from potentially non-phytoplankton-dominated grid cells ( $\text{Rrs}_{555-412 \text{ slope}} \geq \text{boundary value}$ ) by

$$\text{Rrs}_{555-412 \text{ slope}} = -0.000003\{\log(\text{Chl } a)\}^2 + 0.00002\{\log(\text{Chl } a)\} + 0.00006. \quad (1)$$

Grid cells were considered invalid and masked out if (1)  $\text{Rrs}_{555-412 \text{ slope}} \geq \text{boundary value}$  or (2) Rrs at 555 nm ( $\text{Rrs}_{555}$ )  $> 0.01 \text{ sr}^{-1}$  (or normalized water-leaving radiance  $> 2 \text{ mW cm}^{-2} \mu\text{m}^{-1} \text{ sr}^{-1}$ ; see Siswanto et al., 2011; Moore et al., 2012). This criterion masked 2 % of all Chl *a* data.

The criteria described in the previous paragraph could mask out grid cells with coccolithophore blooms, which are sometimes observed in the Arctic Ocean (e.g., Smyth et al., 2004), as they also have  $\text{Rrs}_{555} > 0.01 \text{ sr}^{-1}$  (Moore et al., 2012). Unlike waters dominated by non-phytoplankton particles, whose Rrs spectral shape peaks at 555 nm, the Rrs spectral shape of waters with coccolithophore blooms peaks at 490 or 510 nm (see Iida et al., 2002; Moore et al., 2012). Therefore, grid cells with Rrs spectral peaks at 490 or 510 nm (already classified using the criteria of Rrs at 490 nm ( $\text{Rrs}_{490}$ )  $>$  Rrs at 443 nm ( $\text{Rrs}_{443}$ ) and Rrs at 510 nm ( $\text{Rrs}_{510}$ )  $>$   $\text{Rrs}_{555}$ ) were considered as coccolithophore grid cells and were reintroduced. Of the masked Chl *a* data, 8 % were reintroduced by this criterion.

#### 3.2 Chlorophyll *a* interpolation

Chl *a* values are often missing because of cloud cover, low angle of sunlight, or sea ice. For the period and area analyzed here, data are missing for 86 % of the space and time grid cells. Because  $p\text{CO}_{2w}$  mapping requires a complete Chl *a* field without missing values, we interpolated the Chl *a* data as follows; (1) Chl *a* was set to  $0.01 \text{ mg m}^{-3}$  (minimum value of Chl *a*) in high-latitude regions in winter when there was no light (north of  $80^\circ \text{ N}$  in December and January, and north of  $88^\circ \text{ N}$  in November and February). (2) Whenever SIC was greater than 99 %, Chl *a* was set to  $0.01 \text{ mg m}^{-3}$  (full ice coverage, thus minimum Chl *a*). We chose the strict criterion of  $\text{SIC} > 99 \%$  because weak but significant primary production has been found to occur under the sea ice in regions with SIC around 90 % (Gosselin et al., 1997; Ulfsbo et al., 2014; Assmy et al., 2017). (3) The remaining grid cells with missing data were filled, wherever possible, using the average of Chl *a* in the surrounding grid cells within  $\pm 1^\circ$  latitude and

$\pm 1^\circ$  longitude; this mainly compensated for missing Chl *a* values due to cloud cover or grid cells masked out as potentially affected by CDOM and TSM. (4) Parts of the remaining missing Chl *a* values, mainly for the pre-satellite period of January–August 1997, were set to the monthly climatological Chl *a* values based on the 18-year monthly mean from 1997 to 2014. (5) The final remaining missing Chl *a* data, mainly for the marginal sea ice zone, were generated with linear interpolation using surrounding data. With each interpolation step the number of grid cells with missing data decreased; 23 % of grid cells without Chl *a* data were filled by the first step, and the subsequent steps provided data for the remaining 12, 8, 5, and 52 %.

### 3.3 Gridding of $p\text{CO}_2$ data

In order to bring the individual  $p\text{CO}_{2\text{w}}$  data to the same resolution as the other input data, they were gridded to  $1^\circ \times 1^\circ \times 1$  month grid cells covering the years from 1997 to 2014. This was carried out using the same three-step procedure of Yasunaka et al. (2016) as this excludes values that deviate strongly from the long-term mean in the area of each grid cell. In short, first, anomalous values were screened in the following manner. We calculated the long-term mean and its standard deviation for a window size of  $\pm 5^\circ$  of latitude,  $\pm 30^\circ$  of longitude, and  $\pm 2$  months (regardless of the year) for each  $1^\circ \times 1^\circ \times 1$  month grid cell. We then eliminated the data in each grid cell that differed by more than 3 standard deviations from this long-term mean. In the second step, we recalculated the long-term mean and its standard deviation using a smaller window size of  $\pm 2^\circ$  of latitude,  $\pm 10^\circ$  of longitude, and  $\pm 1$  month (regardless of the year) for each  $1^\circ \times 1^\circ \times 1$  month grid cell, and eliminated data that differed from that long-term mean by more than 3 standard deviations. In the final step the mean value of the remaining data in each  $1^\circ \times 1^\circ \times 1$  month grid cell for each year from 1997 to 2014 was calculated. This procedure identified in total about 0.5 % of the data as extreme values. These may well be correct observations, but likely reflect small spatial scale and/or short timescale variations that can be quite atypical of the large-scale variability of interest in this study. These excluded values were randomly distributed in time and space.

Although some studies have used  $p\text{CO}_{2\text{w}}$  normalized to a certain year, based on the assumption of a constant rate of increase for  $p\text{CO}_{2\text{w}}$  (e.g., Takahashi et al., 2009), we used “non-normalized”  $p\text{CO}_{2\text{w}}$  values from all years; therefore, in our analysis  $p\text{CO}_{2\text{w}}$  can increase both nonlinearly in time and non-uniformly in space.

### 3.4 $p\text{CO}_2$ estimation using a self-organizing map

We estimated  $p\text{CO}_{2\text{w}}$  using the SOM technique used by Yasunaka et al. (2016), but with Chl *a* as an added training parameter to the SOM in addition to SST, SSS, SIC,  $x\text{CO}_{2\text{a}}$ , and geographical position  $X$  ( $= \sin[\text{latitude}] \times \cos[\text{longitude}]$ )

and  $Y$  ( $= \sin[\text{latitude}] \times \sin[\text{longitude}]$ ). Chl *a*, SST, SSS, and SIC are closely associated with processes causing variation in  $p\text{CO}_{2\text{w}}$ , such as primary production, warming–cooling, mixing, and freshwater input, and they represent spatiotemporal  $p\text{CO}_{2\text{w}}$  variability on seasonal to interannual timescales. Including the  $x\text{CO}_{2\text{a}}$  enables the SOM to reflect the  $p\text{CO}_{2\text{w}}$  time trend in response to the atmospheric CO<sub>2</sub> changes including large seasonal variation and continued anthropogenic emissions. In several previous studies the anthropogenic  $p\text{CO}_{2\text{w}}$  increase has been assumed to be steady and homogeneous and subtracted from the original  $p\text{CO}_{2\text{w}}$  data and added to the estimated  $p\text{CO}_{2\text{w}}$  (Nakaoka et al., 2013; Zeng et al., 2014). However, the occurrence of steady and homogeneous  $p\text{CO}_{2\text{w}}$  trends has not yet been demonstrated in the Arctic Ocean and using  $x\text{CO}_{2\text{a}}$  as a training parameter in the SOM, similar to Landschützer et al. (2013, 2014), is preferable. Finally, the inclusion of geographical position among the training parameters can prevent systematic spatial biases (Yasunaka et al., 2014). Compared to other efforts mapping  $p\text{CO}_{2\text{w}}$  using the SOM technique such as those by Telszewski et al. (2009) and Nakaoka et al. (2013), we used  $x\text{CO}_{2\text{a}}$  and geographical position as training parameters while we did not use mixed layer depth because of lack of reliable data in the Arctic.

Briefly, the SOM technique was implemented as follows: first, the approximately 1 million  $1^\circ \times 1^\circ \times 1$  month grid cells in the analysis region and period were assigned to 5000 groups, which are called “neurons”, of the SOM by using the training parameters. Then, each neuron was labeled, whenever possible, with the  $p\text{CO}_{2\text{w}}$  value of the grid cell where the Chl *a*, SST, SSS, SIC,  $x\text{CO}_{2\text{a}}$ , and  $X$  and  $Y$  values were most similar to those of the neuron. Finally, each grid cell in the analysis region and period was assigned the  $p\text{CO}_{2\text{w}}$  value of the neuron whose Chl *a*, SST, SSS, SIC,  $x\text{CO}_{2\text{a}}$ , and  $X$  and  $Y$  values were most similar to those of that grid cell. If the most similar neuron was not labeled with a  $p\text{CO}_{2\text{w}}$  value, then the  $p\text{CO}_{2\text{w}}$  value of the neuron that was most similar and labeled was used. That case often happened in periods and regions without any observed data. A detailed description of the procedure can be found in Telszewski et al. (2009) and Nakaoka et al. (2013).

### 3.5 Calculation of air–sea CO<sub>2</sub> fluxes

We calculated monthly air–sea CO<sub>2</sub> flux ( $F$ ) values from the  $p\text{CO}_{2\text{w}}$  values estimated in Sect. 3.4 by using the bulk formula:

$$F = kL(p\text{CO}_{2\text{w}} - p\text{CO}_{2\text{a}}), \quad (2)$$

where  $k$  is the gas transfer velocity and  $L$  is the solubility of CO<sub>2</sub>. The solubility of CO<sub>2</sub> ( $L$ ) was calculated as a function of SST and SSS (Weiss, 1974). We converted the interpolated NOAA marine boundary layer  $x\text{CO}_{2\text{a}}$  data (Sect. 2.2) to  $p\text{CO}_{2\text{a}}$  by using monthly sea level pressure data and the

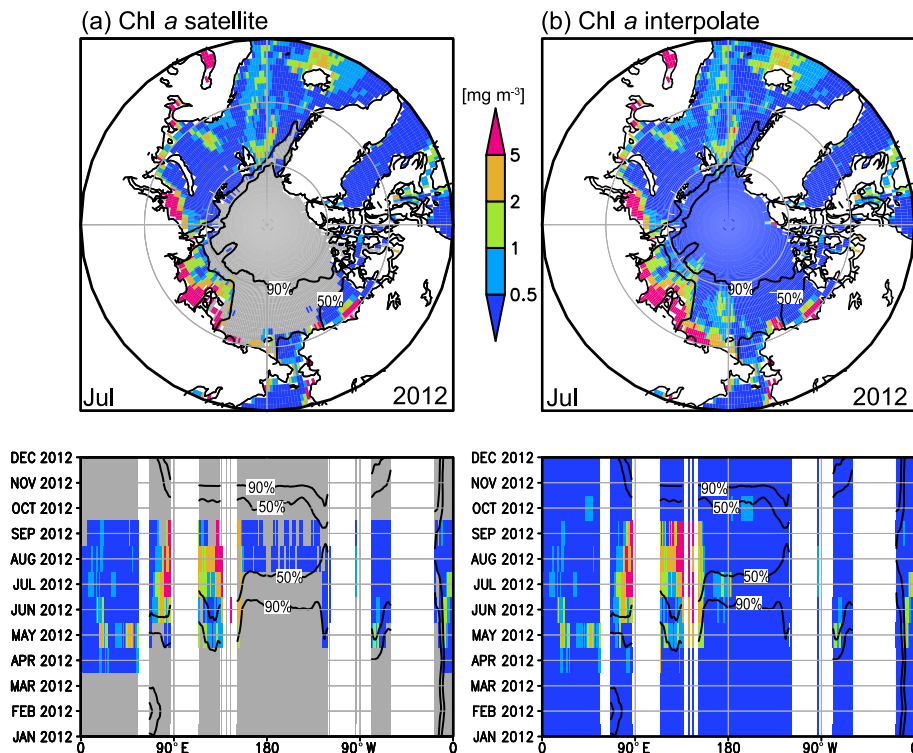


**Figure 3.** (a) Original and (b) interpolated Chl *a* ( $\text{mg m}^{-3}$ ) in July 2012 (upper panels), and along  $75^\circ \text{N}$  in 2012 (lower panels). Black lines denote SIC of 50 and 90 %. Gray areas in (a) indicate missing Chl *a* data.

water vapor saturation pressure calculated from monthly SST and SSS (Murray, 1967).

The gas transfer velocity  $k$  was calculated by using the formula of Sweeney et al. (2007):

$$k = 0.19(S_c/660)^{-0.5} \langle W_{\text{NCEP2}}^2 \rangle, \quad (3)$$

where  $S_c$  is the Schmidt number of CO<sub>2</sub> in seawater at a given SST, calculated according to Wanninkhof (1992, 2014), “ $\langle \rangle$ ” denotes the monthly mean, and  $\langle W_{\text{NCEP2}}^2 \rangle$  is the monthly mean of the second moment of the NCEP2 6-hourly wind speed. The coefficient 0.19, which is the global average of  $0.27 \langle W_{\text{NCEP1}}^2 \rangle / \langle W_{\text{NCEP2}}^2 \rangle$ , is based on the one determined by Sweeney et al. (2007) but optimized for NCEP2 winds, following the same method as Schuster et al. (2013) and Wanninkhof et al. (2013).

The suppression of gas exchange by sea ice was accounted for by correcting the air–sea CO<sub>2</sub> fluxes using the parameterization presented by Loose et al. (2009); the flux is proportional to  $(1 - \text{SIC})^{0.4}$ . Following Bates et al. (2006), in the regions with SIC > 99 %, we used SIC = 99 % to allow for non-negligible rates of air–sea CO<sub>2</sub> exchange through leads, fractures, and brine channels (Semiletov et al., 2004; Fransson et al., 2017). This parameterization reduces the flux in fully ice-covered waters (SIC > 99 %) by 84 %.

## 4 Uncertainty

### 4.1 Uncertainty in chlorophyll *a* concentration data

Figure 3 shows original and interpolated Chl *a* for the year 2012, as an example. Overall, the interpolated Chl *a* data seem to fit well with the original data. Most interpolated Chl *a* data have low concentrations because of high SIC and lack of sunlight. The average of the interpolated Chl *a* values is  $0.1 \text{ mg m}^{-3}$ , and less than 5 % of the interpolated Chl *a* values are  $> 0.5 \text{ mg m}^{-3}$  (cf. the average of the original Chl *a* values is  $1.1 \text{ mg m}^{-3}$ , and 48 % of the original Chl *a* values are  $> 0.5 \text{ mg m}^{-3}$ ). The previous studies to estimate  $p\text{CO}_{2w}$  in high latitudes assumed missing Chl *a* as constant values and ignored spatiotemporal variation in Chl *a* (Landschützer et al., 2013; Nakaoka et al., 2013). However, original Chl *a* values in the ice edge region are not small as captured by Perrette et al. (2011), and those in the northernmost grids in winter, north of which the original Chl *a* values are missing, are far south of the polar night region since they are missing not because of no sunlight but because of low angles of sunlight (Fig. 3a). Therefore, we believe interpolation is better than using low and constant values.

To validate our Chl *a* interpolation, we repeated the interpolation after randomly eliminating 10 % of the satellite Chl *a* values. We then used the eliminated original Chl *a* data as independent data for the validation. Note that this compar-

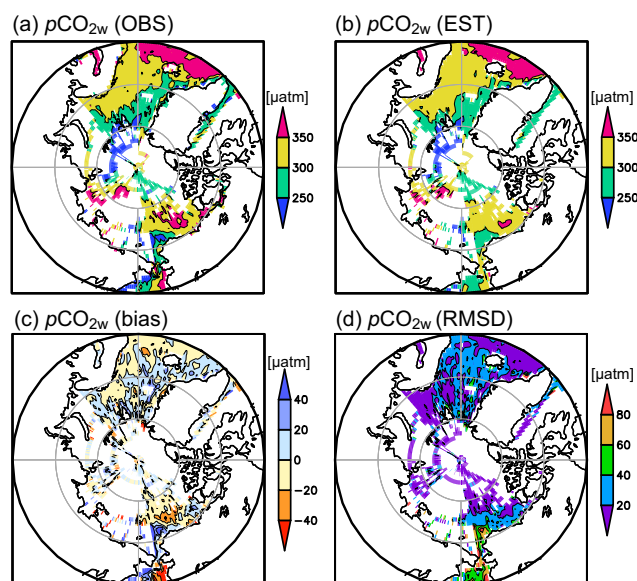


**Figure 4.** (a) Observed  $p\text{CO}_{2w}$  averaged over the whole analysis period ( $\mu\text{atm}$ ). (b) Estimated  $p\text{CO}_{2w}$  averaged over the grid boxes in which observed  $p\text{CO}_{2w}$  values were available ( $\mu\text{atm}$ ). (c) Bias (estimate–observation) and (d) RMSD between observed and estimated  $p\text{CO}_{2w}$  averaged over the whole analysis period ( $\mu\text{atm}$ ).

ison was performed where there were the original Chl *a* data, i.e., the high Chl *a* region. The root mean square difference (RMSD) and correlation coefficient between the interpolated and the independent original Chl *a* data are  $0.90 \text{ mg m}^{-3}$  and 0.80, respectively. It means the interpolated Chl *a*, maybe not quantitatively, but qualitatively reproduced the original Chl *a*, and therefore is a meaningful parameter in the SOM process. Actually Chl *a* data improved the  $p\text{CO}_{2w}$  estimate, even though Chl *a* values in many grid cells were interpolated values (see Sect. 5.4).

To evaluate our choice of Chl *a* algorithm (i.e., the Arctic algorithm of Cota et al., 2004), we compared its calculated Chl *a* values with those determined by using the standard algorithm of O'Reilly et al. (1998) and the coastal algorithm of Tassan (1994). RMSD and correlation coefficient ( $r$ ) between the original (i.e., non-interpolated) Chl *a* values are about  $0.8 \text{ mg m}^{-3}$  and 0.9, respectively (Table 1). For all the Chl *a* values including the interpolated data, they are about  $0.4 \text{ mg m}^{-3}$  and 0.9. The lower RMSD in this case results from the fact that most of the interpolated Chl *a* values have low concentrations. This result means the Chl *a* from the different algorithms are, maybe not quantitatively, but qualitatively consistent with each other. Since not absolute Chl *a* values but relative values affect the  $p\text{CO}_{2w}$  estimates in the SOM technique, the large RMSD among the Chl *a* values does not result in significant difference of the  $p\text{CO}_{2w}$  estimates. Actually, the  $p\text{CO}_{2w}$  and CO<sub>2</sub> fluxes determined using Chl *a* from any of these algorithms as input to the SOM are consistent within their uncertainties (see Sect. 4.2 and 4.3

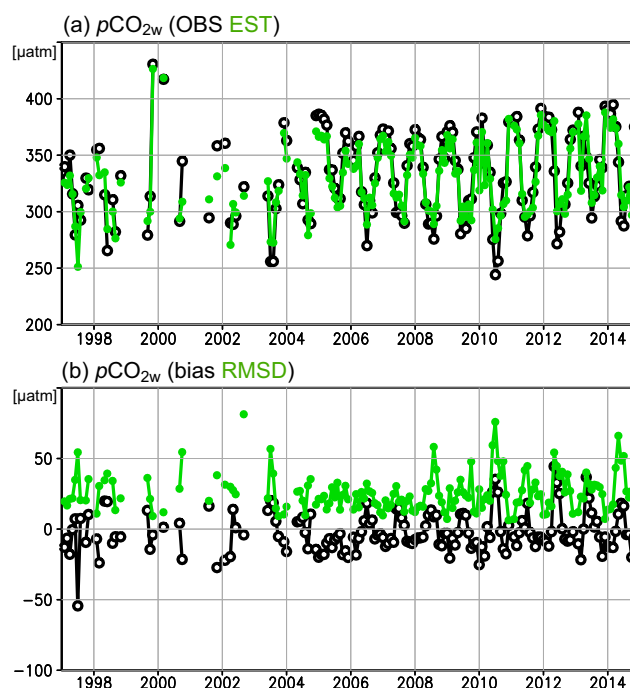


**Figure 5.** (a) Monthly time series of observed  $p\text{CO}_{2w}$  averaged over the entire analysis area (black), and estimated  $p\text{CO}_{2w}$  averaged over the grid boxes in which observed  $p\text{CO}_{2w}$  values were available (green) ( $\mu\text{atm}$ ). (b) Bias (estimate–observation; black) and RMSD (green) between observed and estimated  $p\text{CO}_{2w}$  averaged over the entire analysis area ( $\mu\text{atm}$ ).

below). RMSDs between the observed and estimated  $p\text{CO}_{2w}$  are smallest in the  $p\text{CO}_{2w}$  estimate using Chl *a* from the Arctic algorithm, but the differences are quite small ( $< 1\%$ ).

## 4.2 Uncertainty of $p\text{CO}_{2w}$ mapping

Figure 4 compares observed and estimated  $p\text{CO}_{2w}$  (note that the spatial pattern visible in Fig. 4a and b includes differences generated by different seasonal coverage of data in the various regions). Both observed and estimated  $p\text{CO}_{2w}$  tend to be higher in the subpolar North Atlantic, the Laptev Sea, and the Canada Basin, and lower in the Greenland Sea and the Barents Sea. However, the east–west contrast in the Bering Sea and the contrast between the Canada Basin and the Chukchi Sea are weaker in our estimates than in the observations, and mean bias and RMSD are relatively large in those areas (Fig. 4c and d). The temporal changes in the observed and estimated  $p\text{CO}_{2w}$  are in phase (Fig. 5a), although the variability in the estimated values is somewhat suppressed compared to that of the observed data (note that the temporal change depicted in Fig. 5a also includes changes incurred by time variations in data coverage). The mean bias and RMSD fluctuate seasonally but are at a constant level over the years (Fig. 5b).

**Table 1.** RMSD (mg m<sup>-3</sup>) and correlation (*r*) between Chl *a* values.

	Standard algorithm		Coastal algorithm	
	RMSD	<i>r</i>	RMSD	<i>r</i>
Chl <i>a</i> from Arctic algorithm	0.80	0.90	0.81	0.87
Interpolated Chl <i>a</i> from Arctic algorithm	0.37	0.92	0.48	0.86

The correlation coefficient between estimated and observed  $p\text{CO}_{2\text{w}}$  is 0.82, and the RMSD is 30  $\mu\text{atm}$ , which is 9 % of the average and 58 % of the standard deviation of the observed  $p\text{CO}_{2\text{w}}$  values. This is a performance level categorized as “good” by Maréchal (2004). The differences between the estimated and observed values stem not only from the estimation error but also from the error of the gridded observed data. The uncertainty of the  $p\text{CO}_{2\text{w}}$  measurements is 2–5  $\mu\text{atm}$  (Bakker et al., 2014), the uncertainty of the  $p\text{CO}_{2\text{w}}$  values calculated from DIC and TA, whose uncertainties are within 4 and 6  $\mu\text{mol kg}^{-1}$ , respectively (Olsen et al., 2016), can be up to 14  $\mu\text{atm}$  (Lueker et al., 2000), and the sampling error of the gridded  $p\text{CO}_{2\text{w}}$  observation data was determined from the standard errors of monthly observed  $p\text{CO}_{2\text{w}}$  in the  $1^\circ \times 1^\circ$  grid cells to be 7  $\mu\text{atm}$  (Yasunaka et al., 2016).

To validate our estimated  $p\text{CO}_{2\text{w}}$  values for periods and regions without any observed data, we repeated the mapping experiments after systematically excluding some of the observed  $p\text{CO}_{2\text{w}}$  data when labeling the neurons; four experiments were carried out, by excluding data (1) from 1997 to 2004, (2) from January to April, (3) from north of 80° N, and (4) from the Laptev Sea (90–150° E), where there are only a few  $p\text{CO}_{2\text{w}}$  observations. We compared the  $p\text{CO}_{2\text{w}}$  estimates obtained in each experiment with the excluded observations and found that the  $p\text{CO}_{2\text{w}}$  estimates reproduced the general features of the excluded data, both spatially and temporally (not shown here). They were also similar to the  $p\text{CO}_{2\text{w}}$  estimates obtained by using all observations, although the RMSDs between the estimates and the excluded observations are 54  $\mu\text{atm}$  on average, which is 1.8 times the RMSDs of the estimates based on all observations. It means that our estimated  $p\text{CO}_{2\text{w}}$  values reproduce the general features both in space and time even when and where there are no observed data, although the uncertainty in  $p\text{CO}_{2\text{w}}$  might be as large as 54  $\mu\text{atm}$  in regions and periods without data. We used this uncertainty for  $p\text{CO}_{2\text{w}}$  estimates made by using the  $p\text{CO}_{2\text{w}}$  values of a less similar neuron.

### 4.3 Uncertainty of CO<sub>2</sub> flux estimates

Signorini and McClain (2009) estimated the uncertainty of the CO<sub>2</sub> flux resulting from uncertainties in the gas exchange parameterization to be 36 % and the uncertainty resulting from uncertainties in the wind data to be 11 %. The uncertainty for SIC is 5 % (Cavaliere et al., 1984; Gloersen et al., 1993; Peng et al., 2013). The standard error of

the sea ice effect on gas exchange was estimated to about 30 % by Loose et al. (2009). The uncertainty of  $p\text{CO}_{2\text{a}}$  is about 0.5  $\mu\text{atm}$  (<http://www.esrl.noaa.gov/gmd/ccgg/mbl/mbl.html>), and that of  $p\text{CO}_{2\text{w}}$  was 30  $\mu\text{atm}$  (Sect. 4.2); therefore, we estimated the uncertainty of  $\Delta p\text{CO}_2$  ( $= p\text{CO}_{2\text{w}} - p\text{CO}_{2\text{a}}$ ) to be 34 % (average  $\Delta p\text{CO}_2$  in the analysis domain and period was  $-89 \mu\text{atm}$ ). The overall uncertainty of the estimated CO<sub>2</sub> fluxes is thus 59 % ( $[(0.36^2 + 0.11^2 + 0.05^2 + 0.3^2 + 0.34^2)^{1/2}]$ ) in sea-ice-covered regions and 51 % ( $[(0.36^2 + 0.11^2 + 0.34^2)^{1/2}]$ ) in ice-free regions. For estimates using the  $p\text{CO}_{2\text{w}}$  values of a less similar neuron, whose uncertainty in  $p\text{CO}_{2\text{w}}$  is 54  $\mu\text{atm}$  and the uncertainty of the  $\Delta p\text{CO}_2$  estimates can be as high as 61 %, the uncertainty is 78 % ( $[(0.36^2 + 0.11^2 + 0.05^2 + 0.3^2 + 0.61^2)^{1/2}]$ ) in sea-ice-covered regions and 72 % ( $[(0.36^2 + 0.11^2 + 0.61^2)^{1/2}]$ ) in ice-free regions. The average of the estimated CO<sub>2</sub> flux in the analysis domain and period is 4.8  $\text{mmol m}^{-2} \text{d}^{-1}$ ; hence the uncertainty of the CO<sub>2</sub> flux estimate corresponds to 2.8  $\text{mmol m}^{-2} \text{d}^{-1}$  in sea-ice-covered regions and 2.4  $\text{mmol m}^{-2} \text{d}^{-1}$  in ice-free regions. For estimates using the  $p\text{CO}_{2\text{w}}$  values of a less similar neuron, the uncertainty corresponds to 3.7  $\text{mmol m}^{-2} \text{d}^{-1}$  in the sea-ice-covered region and 3.5  $\text{mmol m}^{-2} \text{d}^{-1}$  in ice-free regions.

## 5 Results and discussion

### 5.1 Relationship between $p\text{CO}_2$ and chlorophyll *a*

Figure 6 compares the observed  $p\text{CO}_{2\text{w}}$  and the original non-interpolated Chl *a* in spring (March–May) and summer (July–September). In spring, when much of the Arctic Ocean is ice covered, Chl *a* is high in the Barents Sea and the Bering Strait ( $> 1 \text{ mg m}^{-3}$ ). In summer, when the ice cover is less extensive, Chl *a* is high in the Chukchi Sea, the Kara Sea, the Laptev Sea, and the East Siberian Sea ( $> 1 \text{ mg m}^{-3}$ ) and especially high in the coastal regions of the two latter ( $> 2 \text{ mg m}^{-3}$ ).  $p\text{CO}_{2\text{w}}$  is high in the Norwegian Sea in spring, and in the Kara Sea, the Laptev Sea, and the Canada Basin during summer ( $> 300 \mu\text{atm}$ ). Conversely, it is lower in the Chukchi Sea, Bering Strait area, and the sea ice edge region of the Eurasian Basin in summer ( $< 300 \mu\text{atm}$ ). The overall correlation between  $p\text{CO}_{2\text{w}}$  and Chl *a* is negative where  $\text{Chl } a \leq 1 \text{ mg m}^{-3}$  (70 % of all the data; correlation coefficient  $r = -0.36$ ,  $P < 0.01$ ), but there is no significant relationship where  $\text{Chl } a > 1 \text{ mg m}^{-3}$  (Fig. 7). A similar situa-

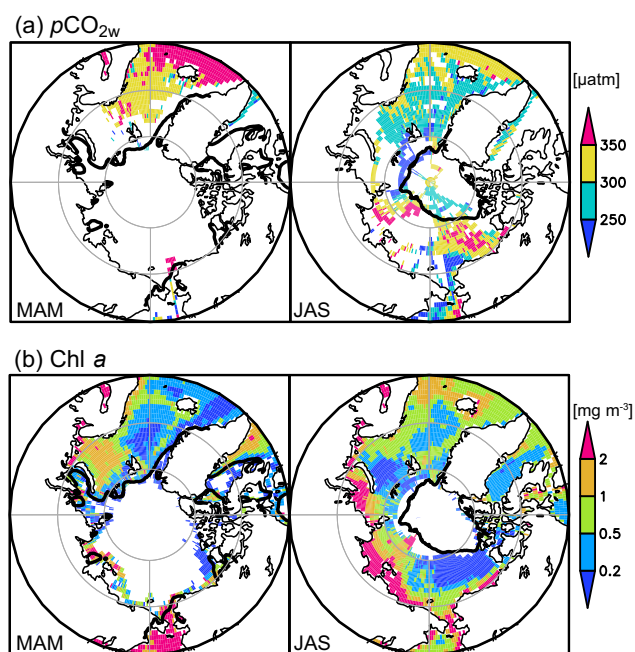


**Figure 6.** (a) Observed  $p\text{CO}_{2w}$  ( $\mu\text{atm}$ ), and (b) non-interpolated Chl  $a$  ( $\text{mg m}^{-3}$ ) in March–May (left) and July–September (right) from 1997 to 2014.

tion was identified in the subpolar North Atlantic by Olsen et al. (2008). It means that primary production generally draws down the  $p\text{CO}_{2w}$ , but high Chl  $a$  values are not necessarily associated with the low  $p\text{CO}_{2w}$  probably because high Chl  $a$  usually appears in the coastal regions (Fig. 6b; see below).

To determine the spatial variability in the relationship between  $p\text{CO}_{2w}$  and Chl  $a$ , we calculated the correlation coefficients between  $p\text{CO}_{2w}$  and Chl  $a$  in a window of  $\pm 5^\circ$  of latitude and  $\pm 30^\circ$  of longitude for each monthly  $1^\circ \times 1^\circ$  grid cell (Fig. 8a). The correlations between  $p\text{CO}_{2w}$  and Chl  $a$  are negative in the Greenland and Norwegian seas and over the Canada Basin. In the Greenland and Norwegian seas, the correlation between  $p\text{CO}_{2w}$  and Chl  $a$  is strongly negative ( $r < -0.4$ ) in spring and weakly negative ( $-0.4 < r < 0$ ) in summer. Chl  $a$  there is higher in summer than in spring (Fig. 6b), whereas nutrient concentrations are high in spring and low in summer (Fig. 8b). Taken together, this suggests that primary production draws down the  $p\text{CO}_{2w}$  in spring, whereas in summer the primary production mostly depends on regenerated nutrients (Harrison and Cota, 1991) and the net CO<sub>2</sub> consumption is small, as also reported for the subpolar North Atlantic (Olsen et al., 2008). Therefore the correlation between  $p\text{CO}_{2w}$  and Chl  $a$  becomes less negative. In the eastern Barents Sea, the Kara Sea and the East Siberian Sea, and the Bering Strait, the correlations are positive because of water with high  $p\text{CO}_{2w}$  and Chl  $a$  in the coastal region subjected to river discharge (Murata, 2006; Semiletov et al., 2007; Anderson et al., 2009; Manizza et al., 2011). In the Chukchi Sea, the relationship is weak ( $-0.2 < r < 0.2$ ),

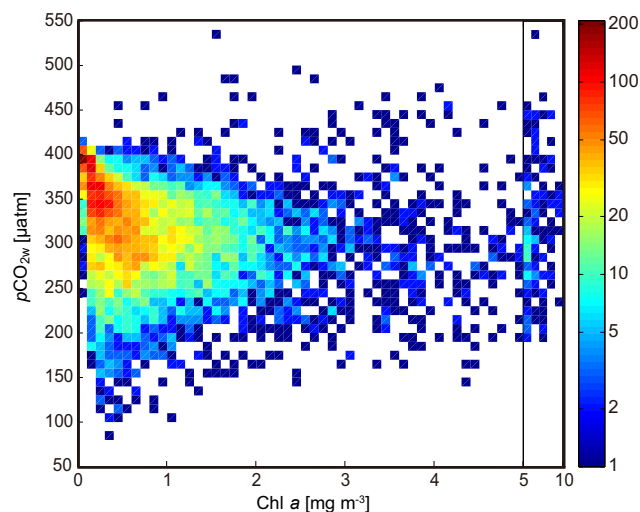


**Figure 7.** Observed  $p\text{CO}_{2w}$  ( $\mu\text{atm}$ ) vs. satellite Chl  $a$  ( $\text{mg m}^{-3}$ ) in the Arctic Ocean and its adjacent seas (north of  $60^\circ\text{N}$ ) from 1997 to 2014. Colors indicate the number of data pairs in a  $0.1 \text{ mg m}^{-3} \times 5 \mu\text{atm}$  bin when Chl  $a \leq 5 \text{ mg m}^{-3}$ , or in a  $1 \text{ mg m}^{-3} \times 5 \mu\text{atm}$  bin when Chl  $a > 5 \text{ mg m}^{-3}$ .

probably because the relationship is on smaller spatial and temporal scales than those represented by the window size used here, as shown by Mucci et al. (2010). The occurrence of calcifying plankton blooms in this region likely also weakens the correlation since the calcification increases  $p\text{CO}_{2w}$  (Shutler et al., 2013; Fransson et al., 2017).

These results show that  $p\text{CO}_{2w}$  relates to Chl  $a$ , but the relationships are different depending on the region and the season. It is difficult to represent such a complex relationship using simple equations (e.g., multiple regression methods) because it needs a priori assumptions of regression functions and of dividing the basin into subregions. But the SOM technique can empirically induce the relationships without any of the a priori assumptions and is therefore suitable to represent such a complex relationship.

## 5.2 Spatiotemporal CO<sub>2</sub> flux variability

The 18-year annual mean CO<sub>2</sub> flux distribution shows that all areas of the Arctic Ocean and its adjacent seas were net CO<sub>2</sub> sinks over the time period that we investigated (Fig. 9). The annual CO<sub>2</sub> influx to the ocean was strong in the Greenland and Norwegian seas ( $9 \pm 3 \text{ mmol m}^{-2} \text{ d}^{-1}$ ; 18-year annual mean  $\pm$  uncertainty averaged over the area shown in Fig. 1), the Barents Sea ( $10 \pm 3 \text{ mmol m}^{-2} \text{ d}^{-1}$ ), and the Chukchi Sea ( $5 \pm 3 \text{ mmol m}^{-2} \text{ d}^{-1}$ ). In contrast, influx was weak and not statistically significantly different from zero in the Eurasian Basin, the Canada Basin, the Laptev Sea, and the East Siberian Sea. Our annual CO<sub>2</sub> flux estimates are consistent with those reported by Yasunaka et al. (2016) and other previous studies (Bates and Mathis, 2009, and references therein).

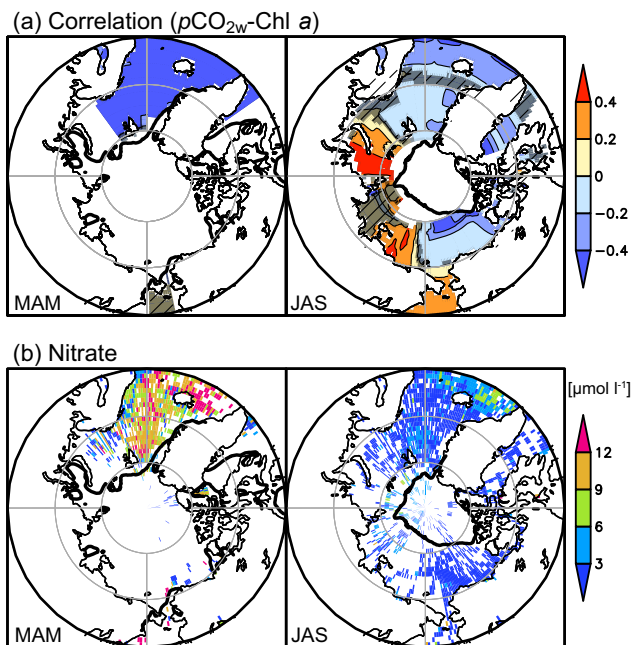


**Figure 8.** (a) Spatial correlation (correlation coefficient,  $r$ ) between  $p\text{CO}_{2w}$  and Chl *a* in a window size of  $\pm 1$  month,  $\pm 5^\circ$  latitude, and  $\pm 30^\circ$  longitude in March–May (left) and July–September (right). Darker hatched areas represent values in grids where correlations are insignificant ( $P > 0.05$ ). (b) Surface nitrate concentration ( $\mu\text{mol l}^{-1}$ ) in March–May (left) and July–September (right) from 1997 to 2014.

The estimated 18-year average CO<sub>2</sub> influx to the Arctic Ocean was  $5 \pm 3 \text{ mmol m}^{-2} \text{ d}^{-1}$ , equivalent to an uptake of  $180 \pm 130 \text{ Tg C yr}^{-1}$  for the ocean area north of  $65^\circ \text{ N}$ , excluding the Greenland and Norwegian seas and Baffin Bay ( $10.7 \times 10^6 \text{ km}^2$ ; see Fig. 1). This accounts for 12 % of the net global CO<sub>2</sub> uptake by the ocean of  $1.5 \text{ Pg C yr}^{-1}$  (Gruber et al., 2009; Wanninkhof et al., 2013; Landschützer et al., 2014). It is within the range of other estimates ( $81$ – $199 \text{ Tg C yr}^{-1}$ ; Bates and Mathis, 2009), but close to the upper bound. That is partly because of the parameterization of the suppression effect by sea ice used in this study. Using another parameterization that represents the SIC effect linearly (Takahashi et al., 2009; Butterworth and Miller, 2016), CO<sub>2</sub> uptake of the Arctic Ocean was estimated to be  $130 \pm 110 \text{ Tg C yr}^{-1}$ .

Figure 10 shows the seasonal variation in the air–sea CO<sub>2</sub> fluxes and its controlling factors ( $\Delta p\text{CO}_2$ , wind speed and SIC; solubility is not shown as the impacts of its variations are relatively small in this context) in the Greenland and Norwegian seas, the Barents Sea, the Chukchi Sea, and the Arctic Ocean. In all of these regions the influxes are strongest in October, when the winds strengthen with the approach of winter and the  $p\text{CO}_{2w}$  and/or SIC are still as low as in the summer. In the Greenland and Norwegian seas and the Barents Sea the CO<sub>2</sub> influx shows a secondary maximum in

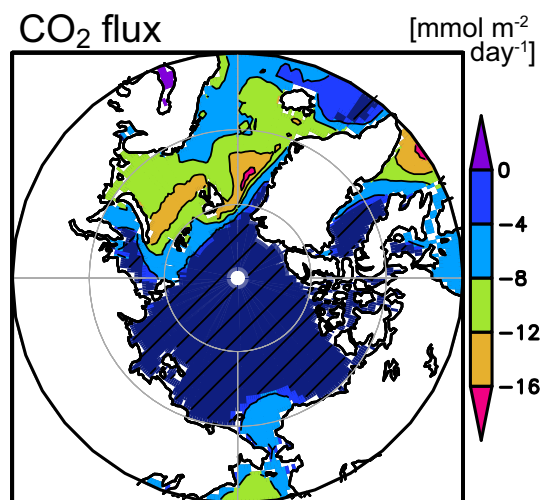


**Figure 9.** The 18-year annual means of CO<sub>2</sub> flux ( $\text{mmol m}^{-2} \text{ day}^{-1}$ ) (negative values indicate flux into the ocean). Darker hatched areas represent values in grids where fluxes were smaller than the uncertainty, estimated as described in the text.

February because the strongest winds occur in that month, while in the Chukchi Sea and Arctic Ocean, the winds are also strong but the flux is suppressed by the extensive sea ice cover. All of these regions are undersaturated with  $p\text{CO}_{2w}$  (i.e., negative  $\Delta p\text{CO}_2$ ) throughout all seasons. The undersaturation is strongest in the Arctic Ocean, as this has the most extensive sea ice cover limiting the fluxes from the atmosphere and the strongest stratification, limiting the mixing of CO<sub>2</sub> rich subsurface waters into the surface ocean. The undersaturation typically shows a maximum (i.e.,  $\Delta p\text{CO}_2$  is minimum) in late spring to early summer (May–June) when the spring bloom occurs (Pabi et al., 2008), but not in the Arctic Ocean. Here the undersaturation reaches its minimum ( $\Delta p\text{CO}_2$  is the smallest) in late summer (August–September) at the time of minimum sea ice cover since the seasonal decrease in  $p\text{CO}_2$  in summer is larger in the air than in the sea. Overall, in the Greenland and Norwegian seas and the Barents Sea the seasonal variations in the CO<sub>2</sub> flux are opposite to those expected from the seasonal  $\Delta p\text{CO}_2$  variations because it is the wind speed that governs most of the seasonal flux variations. In the Chukchi Sea, however, the CO<sub>2</sub> influx is strongest in summer, a consequence of the minimum sea ice cover and strongest  $p\text{CO}_2$  undersaturation. In the Arctic Ocean it is the SIC and wind speed that drive the seasonal flux variations. Seasonal variations in CO<sub>2</sub> flux are consistent with those of the previous studies (Yasunaka et al., 2016, and references therein), whereas seasonal variations in  $p\text{CO}_{2w}$  become realistic (see Sect. 5.3 below).

Figure 11 shows interannual variation in CO<sub>2</sub> flux and its driving factors in these four regions. The interannual variations in CO<sub>2</sub> flux and  $\Delta p\text{CO}_2$  are generally smaller than the seasonal variations and are often smaller than their re-

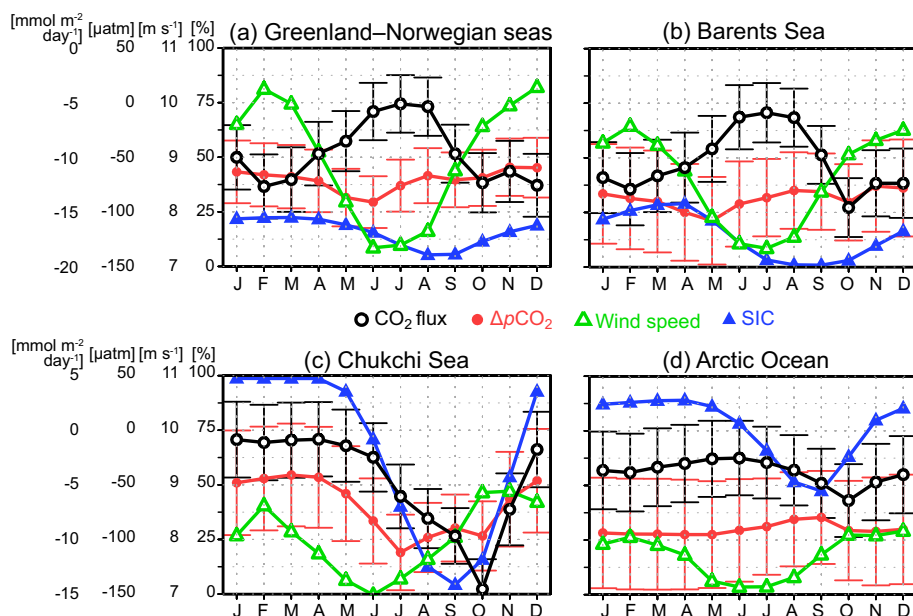


**Figure 10.** The 18-year monthly mean CO<sub>2</sub> flux (mmol m<sup>-2</sup> day<sup>-1</sup>, black), ΔpCO<sub>2</sub> (μatm, red), wind speed (m s<sup>-1</sup>, green), and SIC (%), averaged over (a) the Greenland and Norwegian seas, (b) the Barents Sea, (c) the Chukchi Sea, and (d) the Arctic Ocean. Error bars indicate the uncertainty.

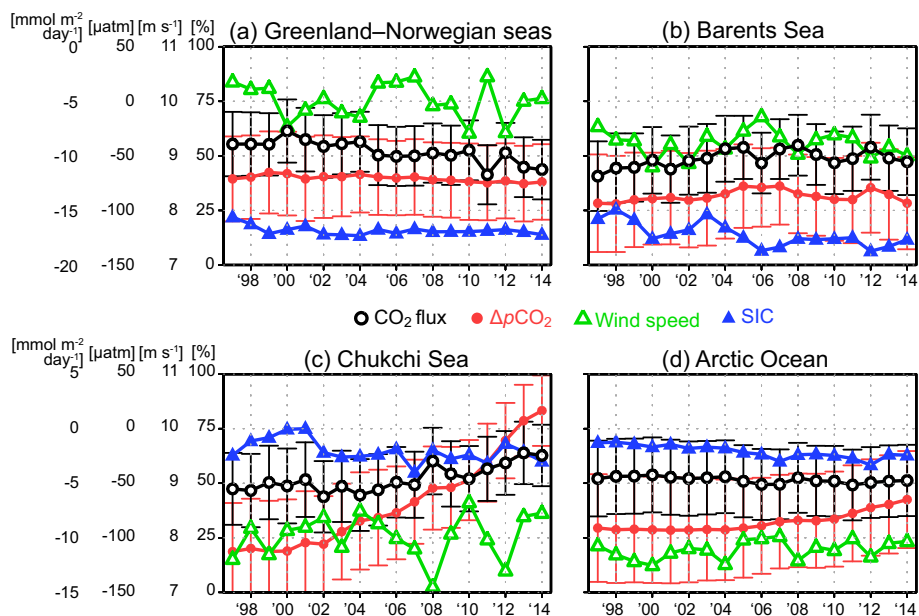


**Figure 11.** Area-mean interannual variations in CO<sub>2</sub> flux (mmol m<sup>-2</sup> day<sup>-1</sup>, black), ΔpCO<sub>2</sub> (μatm, red), wind speed (m s<sup>-1</sup>, green), and SIC (%), blue) in (a) the Greenland and Norwegian seas, (b) the Barents Sea, (c) the Chukchi Sea, and (d) the Arctic Ocean. Error bars indicate the uncertainty.

spective uncertainty. In the Greenland and Norwegian seas, interannual variation in the CO<sub>2</sub> flux negatively correlates with the wind speed (CO<sub>2</sub> influx to the ocean is large when the wind is strong;  $r = -0.41$ ), while interannual variation in ΔpCO<sub>2</sub> and sea ice change is small. In the Barents Sea,

the interannual variation in CO<sub>2</sub> flux positively correlates with ΔpCO<sub>2</sub> ( $r = 0.71$ ) and negatively correlates with SIC ( $r = -0.50$ ), while the correlation with wind speed is not significant. Although low SIC enhances the air–sea CO<sub>2</sub> exchange due to increase in the area of open water, it also as-

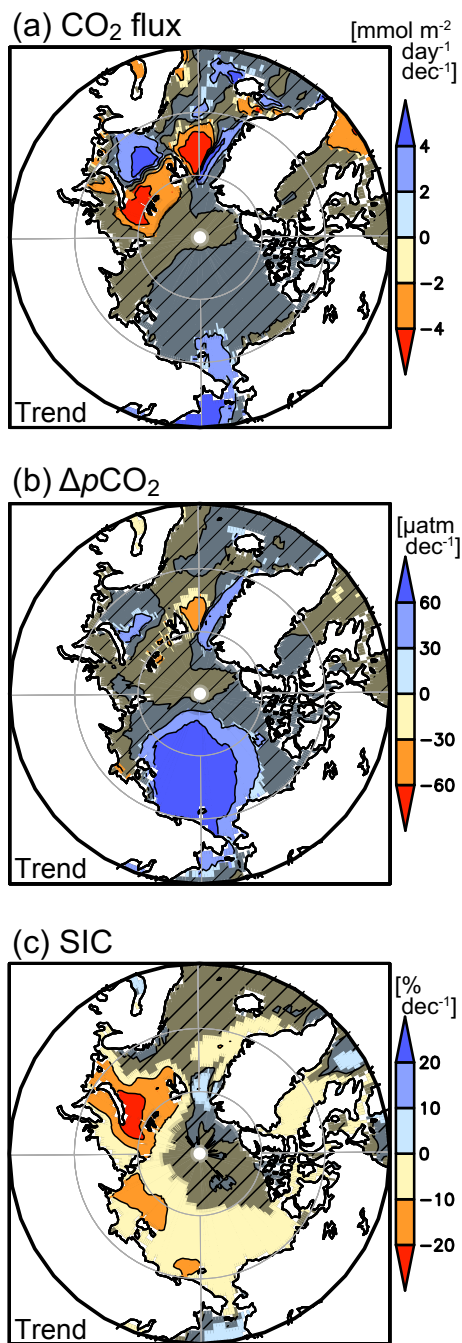


**Figure 12.** Trends in (a) CO<sub>2</sub> flux (mmol m<sup>-2</sup> day<sup>-1</sup> decade<sup>-1</sup>), (b) ΔpCO<sub>2</sub> (μatm decade<sup>-1</sup>), and (c) SIC (% decade<sup>-1</sup>). Darker hatched areas represent values in grids where trend values were less than the uncertainty, estimated as described in the text.

sociates with high SST and therefore high  $p\text{CO}_{2\text{w}}$ . In the Chukchi Sea, CO<sub>2</sub> influx to ocean is decreasing with increasing ΔpCO<sub>2</sub> ( $r = 0.87$ ). High  $p\text{CO}_{2\text{w}}$  (> 500 μatm) via storm-induced deep mixing events has been sometimes observed in the Chukchi Sea after 2010 (Hauri et al., 2013; Taro Takahashi, personal communication, 2017). Interannual

variability in the CO<sub>2</sub> flux averaged over the Arctic Ocean is small because the increasing ΔpCO<sub>2</sub> is compensated for by the effect of sea ice retreat ( $r = -0.70$ ). Thus, the combined effect of sea ice retreat and  $p\text{CO}_{2\text{w}}$  increase on CO<sub>2</sub> flux varied among regions.

The CO<sub>2</sub> influx has been increasing in the Greenland Sea and northern Barents Sea and decreasing in the Chukchi Sea and southern Barents Sea (Fig. 12). The CO<sub>2</sub> flux trend corresponds well with the ΔpCO<sub>2</sub> trend, which in turn corresponds well with the SST trend. The increasing CO<sub>2</sub> influx in the northern Barents Sea also corresponds with the sea ice retreat. These results are similar to those for the previous estimates without using Chl *a* (see Fig. 10 in Yasunaka et al., 2016). It shows again that the combined effect of sea ice retreat and  $p\text{CO}_{2\text{w}}$  increase on the CO<sub>2</sub> flux is regionally different. In the SOM process, the  $p\text{CO}_{2\text{w}}$  values observed in the latter period might be used for the  $p\text{CO}_{2\text{w}}$  estimate in the former period when the  $p\text{CO}_{2\text{w}}$  measurements have not been made, and therefore the trend in CO<sub>2</sub> influx might be affected by the spatiotemporal distribution of the measurements. To confirm this is not the case, we checked that the spatial distribution of the  $p\text{CO}_{2\text{w}}$  trend did not correspond to the year when the first observation was conducted (see Supplement).

### 5.3 Impact of incorporating chlorophyll *a* data in the SOM

To determine the impact of including Chl *a* data in the SOM process, the analyses were repeated without Chl *a* data. The RMSD of the resulting estimated  $p\text{CO}_{2\text{w}}$  values is 33 μatm, which is 3 μatm larger than the uncertainty of the estimates generated by including Chl *a* in the SOM. Chl *a* data thus improved the  $p\text{CO}_{2\text{w}}$  estimate (namely, a 10 % reduction of RMSD), even though 40 % of the Chl *a* data labeled with  $p\text{CO}_{2\text{w}}$  observations were interpolated Chl *a* values.

Figures S1 and S2 in the Supplement present the difference in bias and RMSD for  $p\text{CO}_{2\text{w}}$  estimated with and without Chl *a*; Fig. S1 shows the time evolution and Fig. S2 shows the spatial distribution. Both approaches typically underestimate  $p\text{CO}_{2\text{w}}$  in winter and overestimate the summertime values, but these systematic biases are reduced when Chl *a* values are included in the SOM (Fig. S1). Biases and RMSDs are reduced in the Canada Basin, the western Bering Sea, and the boundary region between the Norwegian Sea and the sub-polar North Atlantic (Fig. S2). As a result, the strong east–west contrast in the Bering Sea and the contrast between the Canada Basin and the Chukchi Sea (see Fig. 4) are better represented when Chl *a* is included. Taken together, inclusion of Chl *a* when estimating  $p\text{CO}_{2\text{w}}$  yields not only better representation of the  $p\text{CO}_{2\text{w}}$  decline in spring and summer but also improves the representation of the spatiotemporal  $p\text{CO}_{2\text{w}}$  distribution. Technically, these improvements come from the fact that Chl *a* as a training parameter can separate high Chl *a* region–time and low Chl *a* region–time into dif-

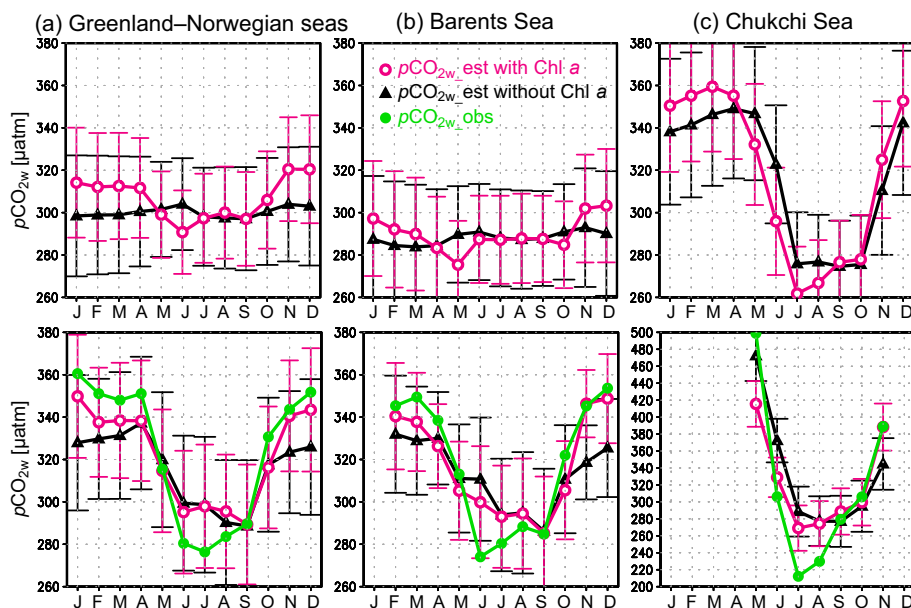


**Figure 13.** The 18-year averaged  $p\text{CO}_{2w}$  seasonal variations ( $\mu\text{atm}$ ) in (a) the Greenland and Norwegian seas, (b) the Barents Sea, and (c) the Chukchi Sea. Black lines with triangles show estimates without Chl *a*; magenta lines with open circles show estimates with Chl *a*; green lines with closed circles show observed values. The upper panels show  $p\text{CO}_{2w}$  averaged for all grid cells within each region, and the lower panels show  $p\text{CO}_{2w}$  averaged over the grid boxes in which observed  $p\text{CO}_{2w}$  values were available. Error bars show the uncertainty, estimated as described in the text.

ferent neurons, which were combined into the same neurons trained without Chl *a*. For example, since Chl *a* is high in spring but SST and SIC are still at similar levels as winter, the grid cells in spring and winter would be classified into separate neurons when Chl *a* is included as a training parameter but in the same neuron when Chl *a* is not included. As a result, without Chl *a*, the estimated  $p\text{CO}_{2w}$  in spring tends to be similar to the  $p\text{CO}_{2w}$  in winter, and the  $p\text{CO}_{2w}$  in winter tends to be similar to that in spring. And therefore the contrast between winter and spring is weakened without Chl *a*.

The seasonal cycles of  $p\text{CO}_{2w}$  estimates derived with the inclusion of Chl *a* have a larger amplitude than the uncertainties, whereas the uncertainties are larger than the seasonal amplitude when  $p\text{CO}_{2w}$  is derived without Chl *a* (upper panels of Fig. 13). The difference is caused by the fact that the seasonal cycle of  $p\text{CO}_{2w}$  in each region reproduces the observed cycle better when Chl *a* was included (lower panels of Fig. 13). Note that the much larger seasonal amplitude in the lower panels is an artefact generated by the seasonal bias in sampling locations; in winter most measurements are obtained at low latitudes where  $p\text{CO}_{2w}$  is typically higher than at high latitudes.

Compared to the CO<sub>2</sub> influx estimates by Yasunaka et al. (2016), the winter CO<sub>2</sub> influx in the Greenland and Norwegian seas estimated including Chl *a* is about  $3 \text{ mmol m}^{-2} \text{ d}^{-1}$  less than that calculated without using Chl *a* (Fig. 14), but this difference is smaller than the uncertainties.

The CO<sub>2</sub> fluxes in the other areas are quite similar for the two estimates, while their uncertainties are smaller in the present estimates.

The inclusion of Chl *a* data also reduced the uncertainty of the estimated annual air–sea CO<sub>2</sub> flux integrated over the entire Arctic Ocean. Compared to the flux estimate determined by Yasunaka et al. (2016) of  $180 \pm 210 \text{ Tg C yr}^{-1}$ , the CO<sub>2</sub> uptake in the Arctic Ocean estimated here is significant within its uncertainty ( $180 \pm 130 \text{ Tg C yr}^{-1}$ ). This improvement is the result of (1) the inclusion of Chl *a* data in the SOM process (which reduced the uncertainty by 23%); (2) the separate uncertainty estimates for ice-free and ice-covered regions (8%); and (3) the addition of new observational  $p\text{CO}_{2w}$  data (7%). Reducing the uncertainty of this quantification is a key contribution to the larger work of constraining the global carbon budget (e.g., Le Quéré et al., 2016). Because the Arctic is an important CO<sub>2</sub> sink, quantifying its fluxes and minimizing the uncertainty is of great scientific value.

#### 5.4 Toward further reduction of the uncertainty

The addition of new observational data from SOCATv4 and GLODAPv2 reduced the overall uncertainty in the mapped  $p\text{CO}_{2w}$ : a 33% increase in the number of observations induced a 7% reduction in the uncertainty. However, there are still few observations in the Kara Sea, the Laptev Sea, the East Siberian Sea, and the Eurasian Basin (Fig. 2). To improve our understanding of the variability in air–sea CO<sub>2</sub>

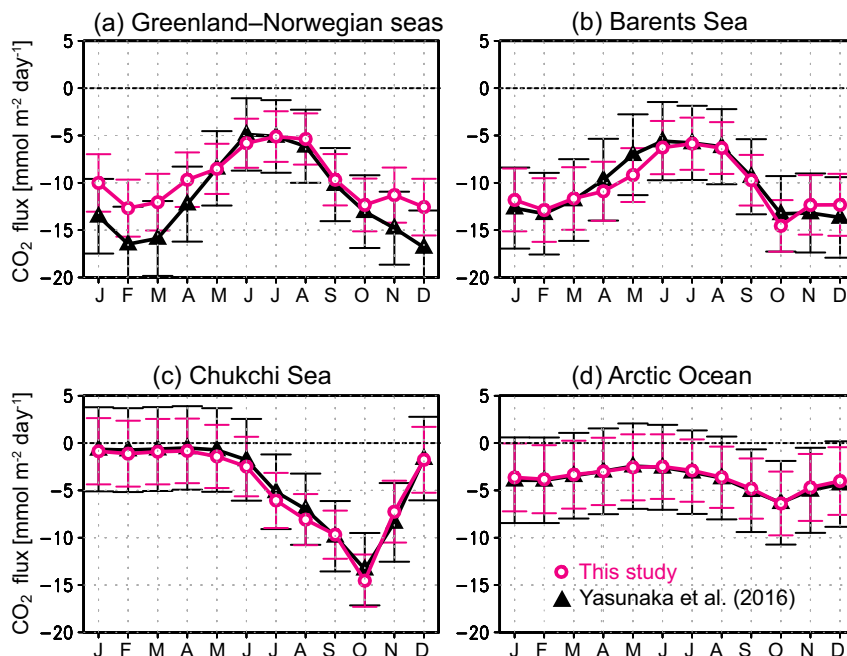


**Figure 14.** The 18-year monthly mean CO<sub>2</sub> flux ( $\text{mmol m}^{-2} \text{day}^{-1}$ ) averaged over (a) the Greenland and Norwegian seas, (b) the Barents Sea, (c) the Chukchi Sea, and (d) the Arctic Ocean. Black lines with triangles show estimates without Chl *a* by Yasunaka et al. (2016); magenta lines with open circles show estimates with Chl *a*. Error bars show the uncertainty, estimated as described in the text.

fluxes in the Arctic, it is of critical importance to obtain additional ocean CO<sub>2</sub> measurements to fill these data gaps and that these measurements are made publically available. Data synthesis activities like SOCAT must be encouraged.

In the present study, we discussed the combined effect of sea ice retreat and  $p\text{CO}_{2w}$  change on the air–sea CO<sub>2</sub> flux. There are other factors that will induce change of CO<sub>2</sub> flux. For example, warmer temperature will lead to an increasing buffering capacity while lower salinity will have the opposite effect and cause a decrease in buffering capacity. In our current study, we used climatological-mean salinity for the  $p\text{CO}_{2w}$  estimate because of lack of reliable year-to-year salinity data. That might be one of the improvements for a future study.

## 6 Conclusions

By applying an SOM technique with the inclusion of Chl *a* data to estimate  $p\text{CO}_{2w}$ , we produced monthly maps of air–sea CO<sub>2</sub> fluxes from 1997 to 2014 for the Arctic Ocean and its adjacent seas north of 60° N. Negative correlation between  $p\text{CO}_{2w}$  and Chl *a* meant that Chl *a* is a valuable parameter to represent primary production. Since the relationship varied among seasons and regions, the SOM technique is better suited for the mapping than a multiple linear regression approach. Adding Chl *a* to the SOM process improved representation of the seasonal cycle of  $p\text{CO}_{2w}$  and therefore reduced the uncertainty of the CO<sub>2</sub> flux estimates.

In the Greenland and Norwegian seas and the Barents Sea the CO<sub>2</sub> influx was large in autumn and winter because of the strong wind. In the Chukchi Sea, however, the CO<sub>2</sub> influx was strong in summer and autumn, as a consequence of the low SIC and strong  $p\text{CO}_{2w}$  undersaturation. Although interannual variation in the CO<sub>2</sub> influx was smaller than the seasonal variation, the CO<sub>2</sub> influx has been increasing in the Greenland Sea and northern Barents Sea and decreasing in the Chukchi Sea and southern Barents Sea.

A major goal of the carbon-cycle research community in recent years has been to reduce the uncertainty in estimates of carbon reservoirs and fluxes. Our results contribute to this in that CO<sub>2</sub> uptake in the Arctic Ocean is demonstrated with high significance. The resulting estimate of the annual Arctic Ocean CO<sub>2</sub> uptake of  $180 \text{ Tg C yr}^{-1}$  is significant with an uncertainty of  $\pm 130 \text{ Tg C yr}^{-1}$ . This is a substantial improvement over earlier estimates and is due mainly to the incorporation of Chl *a* data.

Assessment of the numerical models using our estimate of Arctic carbon uptake is also an interesting topic since numerical models are poorly validated in the Arctic due to the limited observations of biogeochemistry (Popova et al., 2012). However, such experiments need thorough insight into the numerical models, which is beyond the scope of this study. We hope to perform such comparisons in future studies.

**Data availability.** The monthly CO<sub>2</sub> flux, pCO<sub>2w</sub>, and interpolated Chl *a* data presented in this paper will be available at the JAMSTEC website (<http://www.jamstec.go.jp/res/ress/yasunaka/co2flux/>, Yasunaka, 2018).

**Supplement.** The supplement related to this article is available online at: <https://doi.org/10.5194/bg-15-1643-2018-supplement>.

**Competing interests.** The authors declare that they have no conflict of interest.

**Acknowledgements.** We thank the many researchers and funding agencies responsible for the collection of data and quality control for their contributions to SOCAT and GLODAPv2. We are grateful for the use of the CO2SYS program obtained from the Ocean Carbon Data System of NOAA National Centers for Environmental Information (<https://www.nodc.noaa.gov/ocads/oceans/CO2SYS/co2rprt.html>), and SOM Toolbox version 2 developed by the Laboratory of Information and Computer Science at Helsinki University of Technology (<http://www.cis.hut.fi/projects/somtoolbox>). We thank ACRI-ST, France, for developing, validating, and distributing the GlobColour data used in this work. This work was financially supported by the Arctic Challenge for Sustainability (ArCS) Project funded by the Ministry of Education, Culture, Sports, Science and Technology, Japan. Are Olsen was supported by grants from the Norwegian Research Council (Subpolar North Atlantic Climate States (SNACS) 229752 and the Norwegian component of the Integrated Carbon Observation System (ICOS-Norway 245927). Mario Hoppema was partly supported by the German Federal Ministry of Education and Research (grant no. 01LK1224I; ICOS-D). Siv K. Lauvset acknowledges support from the Norwegian Research Council (VENTILATE, 229791) and the EU H2020 project AtlantOS (grant agreement no. 633211). Rik Wanninkhof and Taro Takahashi acknowledge support from the Office of Oceanic and Atmospheric Research (OAR) of NOAA, including resources from the Ocean Observation and Monitoring Division of the Climate Program Office (fund reference 100007298). We thank two anonymous reviewers for providing helpful comments.

Edited by: Alexey V. Eliseev

Reviewed by: two anonymous referees

## References

- Anderson, L. G., Jutterström, S., Hjalmarsen, S., Wählström, I., and Semiletov, I. P.: Out-gassing of CO<sub>2</sub> from Siberian Shelf seas by terrestrial organic matter decomposition, *Geophys. Res. Lett.*, 36, L20601, <https://doi.org/10.1029/2009GL040046>, 2009.
- Ardyna, M., Babin, M., Gosselin, M., Devred, E., Rainville, L., and Tremblay, J.-É.: Recent Arctic Ocean sea ice loss triggers novel fall phytoplankton blooms, *Geophys. Res. Lett.*, 41, 6207–6212, <https://doi.org/10.1002/2014GL061047>, 2014.
- Arrigo, K. R. and van Dijken, G. L.: Annual cycles of sea ice and phytoplankton near Cape Bathurst, southeastern Beau-
- fort Sea, Canadian Arctic, *Geophys. Res. Lett.*, 31, L08304, <https://doi.org/10.1029/2003GL018978>, 2004.
- Assmy P. M. Fernandez-Mendez, Duarte, P., Meyer, A., Randelhoff, A., Mundy, C. J., Olsen, L. M., Kauko, H. M., Bailey, A., Chierici, M., Cohen, L., Doulgeris, A. P., Ehn, J. K., Fransson, A., Gerland, S., Hop, H., Hudson, S. R., Hughes, N., Itkin, P., Johnsen, G., King, J. A., Koch, B. P., Koenig, Z., Kwasniewski, S., Laney, S. R., Nicolaus, M., Pavlov, A. K., Polashenski, C. M., Provost, C., Rösel, A., Sandbu, M., Spreen, G., Smedsrud, L. H., Sundfjord, A., Taskjelle, T., Tatarek, A., Wiktor, J., Wagner, P. M., Wold, A., Steen, H., and Granskog, M. A.: Leads in Arctic pack ice enable early phytoplankton blooms below snow-covered sea ice, *Scientific Report*, 7, 40850, <https://doi.org/10.1038/srep40850>, 2017.
- Bakker, D. C. E., Pfeil, B., Smith, K., Hankin, S., Olsen, A., Alin, S. R., Cosca, C., Harasawa, S., Kozyr, A., Nojiri, Y., O'Brien, K. M., Schuster, U., Telszewski, M., Tilbrook, B., Wada, C., Akl, J., Barbero, L., Bates, N. R., Boutin, J., Bozec, Y., Cai, W.-J., Castle, R. D., Chavez, F. P., Chen, L., Chierici, M., Currie, K., de Baar, H. J. W., Evans, W., Feely, R. A., Fransson, A., Gao, Z., Hales, B., Hardman-Mountford, N. J., Hoppema, M., Huang, W.-J., Hunt, C. W., Huss, B., Ichikawa, T., Johannessen, T., Jones, E. M., Jones, S. D., Jutterström, S., Kitidis, V., Körtzinger, A., Landschützer, P., Lauvset, S. K., Lefèvre, N., Manke, A. B., Mathis, J. T., Merlivat, L., Metzl, N., Murata, A., Newberger, T., Omar, A. M., Ono, T., Park, G.-H., Paterson, K., Pierrot, D., Ríos, A. F., Sabine, C. L., Saito, S., Salisbury, J., Sarma, V. V. S. S., Schlitzer, R., Sieger, R., Skjelvan, I., Steinhoff, T., Sullivan, K. F., Sun, H., Sutton, A. J., Suzuki, T., Sweeney, C., Takahashi, T., Tjiputra, J., Tsurushima, N., van Heuven, S. M. A. C., Vandemark, D., Vlahos, P., Wallace, D. W. R., Wanninkhof, R., and Watson, A. J.: An update to the Surface Ocean CO<sub>2</sub> Atlas (SOCAT version 2), *Earth Syst. Sci. Data*, 6, 69–90, <https://doi.org/10.5194/essd-6-69-2014>, 2014.
- Bakker, D. C. E., Pfeil, B., Landa, C. S., Metzl, N., O'Brien, K. M., Olsen, A., Smith, K., Cosca, C., Harasawa, S., Jones, S. D., Nakaoka, S.-I., Nojiri, Y., Schuster, U., Steinhoff, T., Sweeney, C., Takahashi, T., Tilbrook, B., Wada, C., Wanninkhof, R., Alin, S. R., Balestrini, C. F., Barbero, L., Bates, N. R., Bianchi, A. A., Bonou, F., Boutin, J., Bozec, Y., Burger, E. F., Cai, W.-J., Castle, R. D., Chen, L., Chierici, M., Currie, K., Evans, W., Featherstone, C., Feely, R. A., Fransson, A., Goyet, C., Greenwood, N., Gregor, L., Hankin, S., Hardman-Mountford, N. J., Harlay, J., Hauck, J., Hoppema, M., Humphreys, M. P., Hunt, C. W., Huss, B., Ibáñez, J. S. P., Johannessen, T., Keeling, R., Kitidis, V., Körtzinger, A., Kozyr, A., Krasakopoulou, E., Kuwata, A., Landschützer, P., Lauvset, S. K., Lefèvre, N., Lo Monaco, C., Manke, A., Mathis, J. T., Merlivat, L., Millero, F. J., Monteiro, P. M. S., Munro, D. R., Murata, A., Newberger, T., Omar, A. M., Ono, T., Paterson, K., Pearce, D., Pierrot, D., Robbins, L. L., Saito, S., Salisbury, J., Schlitzer, R., Schneider, B., Schweitzer, R., Sieger, R., Skjelvan, I., Sullivan, K. F., Sutherland, S. C., Sutton, A. J., Tadokoro, K., Telszewski, M., Tuma, M., van Heuven, S. M. A. C., Vandemark, D., Ward, B., Watson, A. J., and Xu, S.: A multi-decade record of high-quality *f*CO<sub>2</sub> data in version 3 of the Surface Ocean CO<sub>2</sub> Atlas (SOCAT), *Earth Syst. Sci. Data*, 8, 383–413, <https://doi.org/10.5194/essd-8-383-2016>, 2016.
- Bates, N. R. and Mathis, J. T.: The Arctic Ocean marine carbon cycle: evaluation of air–sea CO<sub>2</sub> exchanges, ocean acidification

- impacts and potential feedbacks, *Biogeosciences*, 6, 2433–2459, <https://doi.org/10.5194/bg-6-2433-2009>, 2009.
- Bates, N. R., Moran, S. B., Hansell, D. A., and Mathis, J. T.: An increasing CO<sub>2</sub> sink in the Arctic Ocean due to sea-ice loss, *Geophys. Res. Lett.*, 33, L23609, <https://doi.org/10.1029/2006GL027028>, 2006.
- Bates, N. R., Garley, R., Frey, K. E., Shake, K. L., and Mathis, J. T.: Sea-ice melt CO<sub>2</sub>-carbonate chemistry in the western Arctic Ocean: meltwater contributions to air–sea CO<sub>2</sub> gas exchange, mixed-layer properties and rates of net community production under sea ice, *Biogeosciences*, 11, 6769–6789, <https://doi.org/10.5194/bg-11-6769-2014>, 2014.
- Boyer, T. P., Antonov, J. I., Baranova, O. K., Coleman, C., Garcia, H. E., Grodsky, A., Johnson, D. R., Locarnini, R. A., Mishonov, A. V., O'Brien, T. D., Paver, C. R., Reagan, J. R., Seidov, D., Smolyar, I. V., and Zweng, M. M.: *World Ocean Database 2013*, Sydney Levitus, edited by: Mishonov, A., NOAA Atlas NESDIS 72, 209 pp., 2013.
- Butterworth, B. J. and Miller, S. D.: Air-sea exchange of carbon dioxide in the Southern Ocean and Antarctic marginal ice zone, *Geophys. Res. Lett.*, 43, 7223–7230, <https://doi.org/10.1002/2016GL069581>, 2016.
- Cai, W. J., Chen, L. Q., Chen, B. S., Gao, Z. Y., Lee, S. H., Chen, J. F., Pierrot, D., Sullivan, K., Wang, Y. C., Hu, X. P., Huang, W. J., Zhang, Y. H., Xu, S. Q., Murata, A., Grebmeier, J. M., Jones, E. P., and Zhang, H. S.: Decrease in the CO<sub>2</sub> uptake capacity in an ice-free Arctic Ocean Basin, *Science*, 329, 556–559, <https://doi.org/10.1126/science.1189338>, 2010.
- Cavaliere, D. J., Gloersen, P., and Campbell, W. J.: Determination of sea ice parameters with the NIMBUS-7 SMMR, *J. Geophys. Res.*, 89, 5355–5369, 1984.
- Chierici, M., Olsen, A., Johannessen, T., Trinañes, J., and Wanninkhof, R.: Algorithms to estimate CO<sub>2</sub> in the northern North Atlantic using observations, satellite and ocean analysis data, *Deep-Sea Res. II*, 56, 630–639, <https://doi.org/10.1016/j.dsr2.2008.12.014>, 2009.
- Chierici, M., Fransson, A., Lansard, B., Miller, L. A., Mucci, A., Shadwick, E., Thomas, H., Tremblay, J.-E., and Papakyriakou, T.: The impact of biogeochemical processes and environmental factors on the calcium carbonate saturation state in the Circumpolar Flaw Lead in the Amundsen Gulf, Arctic Ocean, *J. Geophys. Res.*, 116, C00G09, <https://doi.org/10.1029/2011JC007184>, 2011.
- Conway, T. J., Tans, P. P., Waterman, L. S., Thoning, K. W., Kitzis, D. R., Masarie, K. A., and Zhang, N.: Evidence for interannual variability of the carbon cycle from the NOAA/CMDL global air sampling network, *J. Geophys. Res.*, 99, 22831–22855, 1994.
- Cota, G. F., Wang, J., and Comiso, J. C.: Transformation of global satellite chlorophyll retrievals with a regionally tuned algorithm, *Remote Sens. Environ.*, 89, 326–350, <https://doi.org/10.1016/j.rse.2004.01.005>, 2004.
- Dickson, A. G.: Standard potential of the reaction:  $\text{AgCl(s)} + 1/2\text{H}_2(\text{g}) = \text{Ag(s)} + \text{HCl(aq)}$ , and the standard acidity constant of the ion  $\text{HSO}_4^-$  in synthetic seawater from 273.15 to 318.15 K, *J. Chem. Thermodyn.*, 22, 113–127, 1990.
- Else, B. G. T., Galley, R. J., Lansard, B., Barber, D. G., Brown, K., Miller, L. A., Mucci, A., Papakyriakou, T. N., Tremblay, J.-É., and Rysgaard, S.: Further observations of a decreasing atmospheric CO<sub>2</sub> uptake capacity in the Canada Basin (Arctic Ocean) due to sea ice loss, *Geophys. Res. Lett.*, 40, 1132–1137, <https://doi.org/10.1002/grl.50268>, 2013.
- Fransson, A., Chierici, M., Skjelvan, I., Olsen, A., Assmy, P., Peterson, A. K., Spreen, G., and Ward, B.: Effects of sea-ice and biogeochemical processes and storms on under-ice water *f*CO<sub>2</sub> during the winter-spring transition in the high Arctic Ocean: Implications for sea-air CO<sub>2</sub> fluxes, *J. Geophys. Res.*, 122, 5566–5587, <https://doi.org/10.1002/2016JC012478>, 2017.
- Gao, Z., Chen, L., Sun, H., Chen, B., and Cai, W.-J.: Distributions and air–sea fluxes of carbon dioxide in the Western Arctic Ocean, *Deep-Sea Res. II*, 81–84, 46–52, <https://doi.org/10.1016/j.dsr2.2012.08.021>, 2012.
- Gloersen, P., Campbell, W. J., Cavalieri, D. J., Comiso, J. C., Parkinson, C. L., and Zwally, H. J.: Arctic and Antarctic sea ice, 1978–1987: Satellite passive-microwave observations and analysis, *NASA Spec. Publ.*, 511, 290 pp., 1993.
- Gosselin, M., Levasseur, M., Wheeler, P. A., Horner, R. A., and Booth, B. C.: New measurements of phytoplankton and ice algal production in the Arctic Ocean, *Deep-Sea Res. II*, 44, 1623–1644, [https://doi.org/10.1016/S0967-0645\(97\)00054-4](https://doi.org/10.1016/S0967-0645(97)00054-4), 1997.
- Gruber, N., Gloor, M., Mikaloff Fletcher, S. E., Dutkiewicz, S., Follows, M., Doney, S. C., Gerber, M., Jacobson, A. R., Lindsay, K., Menemenlis, D., Mouchet, A., Mueller, S. A., Sarmiento, J. L., and Takahashi, T.: Oceanic sources and sinks for atmospheric CO<sub>2</sub>, *Global Biogeochem. Cy.*, 23, GB1005, <https://doi.org/10.1029/2008GB003349>, 2009.
- Harrison, W. G. and Cota, G. F.: Primary production in polar waters: relation to nutrient availability, *Polar Res.*, 10, 87–104, <https://doi.org/10.1111/j.1751-8369.1991.tb00637.x>, 1991.
- Hauri, C., Winsor, P., Juraneck, L. W., McDonnell, A. M. P., Takahashi, T., and Mathis, J. T.: Wind-driven mixing causes a reduction in the strength of the continental shelf carbon pump in the Chukchi Sea, *Geophys. Res. Lett.*, 40, 5932–5936, <https://doi.org/10.1002/2013GL058267>, 2013.
- Iida, T., Saitoh, S. I., Miyamura, T., Toratani, M., Fukushima, H., and Shiga, N.: Temporal and spatial variability of coccolithophore blooms in the eastern Bering Sea, 1998–2001, *Prog. Oceanogr.*, 55, 165–175, 2002.
- Kalnay, E., Kanamitsu, M., Kistler, R., Collins, W., Deaven, D., Gandin, L., Iredell, M., Saha, S., White, G., Woollen, J., Zhu, Y., Chelliah, M., Ebisuzaki, W., Higgins, W., Janowiak, J., Mo, K. C., Ropelewski, C., Wang, J., Leetmaa, A., Reynolds, R., Jenne, R., and Joseph, D.: The NCEP/NCAR 40-Year Reanalysis Project, *B. Am. Meteorol. Soc.*, 77, 437–71, 1996.
- Kanamitsu, M., Ebisuzaki, W., Woollen, J., Yang, S.-K., Hnilo, J. J., Fiorino, M., and Potter, G. L.: NCEP-DOE AMIP-II Reanalysis (R-2), *B. Am. Meteorol. Soc.*, 83, 1631–1643, 2002.
- Key, R. M., Olsen, A., van Heuven, S., Lauvset, S. K., Velo, A., Lin, X., Schirnick, C., Kozyr, A., Tanhua, T., Hoppema, M., Jutterström, S., Steinfeldt, R., Jeansson, E., Ishii, M., Perez, F. F., and Suzuki, T.: Global Ocean Data Analysis Project, Version 2 (GLODAPv2), ORNL/CDIAC-162, ND-P093, Carbon Dioxide Information Analysis Center, Oak Ridge National Laboratory, US Department of Energy, Oak Ridge, Tennessee, [https://doi.org/10.3334/CDIAC/OTG.NDP093\\_GLODAPv2](https://doi.org/10.3334/CDIAC/OTG.NDP093_GLODAPv2), 2015.
- Landschützer, P., Gruber, N., Bakker, D. C. E., Schuster, U., Nakaoka, S., Payne, M. R., Sasse, T. P., and Zeng, J.: A neural network-based estimate of the seasonal to inter-annual vari-

- ability of the Atlantic Ocean carbon sink, *Biogeosciences*, 10, 7793–7815, <https://doi.org/10.5194/bg-10-7793-2013>, 2013.
- Landschützer, P., Gruber, N., Bakker, D. C. E., and Schuster, U.: Recent variability of the global ocean carbon sink, *Global Biogeochem. Cycles*, 28, 927–949, <https://doi.org/10.1002/2014GB004853>, 2014.
- Lefèvre, N., Watson, A. J., and Watson, A. R.: A comparison of multiple regression and neural network techniques for mapping in situ pCO<sub>2</sub> data, *Tellus B*, 57, 375–384, <https://doi.org/10.1111/j.1600-0889.2005.00164.x>, 2005.
- Le Quééré, C., Andrew, R. M., Canadell, J. G., Sitch, S., Korsbakken, J. I., Peters, G. P., Manning, A. C., Boden, T. A., Tans, P. P., Houghton, R. A., Keeling, R. F., Alin, S., Andrews, O. D., Anthoni, P., Barbero, L., Bopp, L., Chevallier, F., Chini, L. P., Ciais, P., Currie, K., Delire, C., Doney, S. C., Friedlingstein, P., Gkritzalis, T., Harris, I., Hauck, J., Haverd, V., Hoppema, M., Klein Goldewijk, K., Jain, A. K., Kato, E., Körtzinger, A., Landschützer, P., Lefèvre, N., Lenton, A., Lienert, S., Lombardozi, D., Melton, J. R., Metzl, N., Millero, F., Monteiro, P. M. S., Munro, D. R., Nabel, J. E. M. S., Nakaoka, S.-I., O'Brien, K., Olsen, A., Omar, A. M., Ono, T., Pierrot, D., Poulter, B., Rödenbeck, C., Salisbury, J., Schuster, U., Schwinger, J., Séférian, R., Skjelvan, I., Stocker, B. D., Sutton, A. J., Takahashi, T., Tian, H., Tilbrook, B., van der Laan-Luijkx, I. T., van der Werf, G. R., Viovy, N., Walker, A. P., Wiltshire, A. J., and Zaehle, S.: Global Carbon Budget 2016, *Earth Syst. Sci. Data*, 8, 605–649, <https://doi.org/10.5194/essd-8-605-2016>, 2016.
- Lewis, E. and Wallace, D. W. R.: Program Developed for CO<sub>2</sub> System Calculations. ORNL/CDIAC-105. Carbon Dioxide Information Analysis Center, Oak Ridge National Laboratory, U.S. Department of Energy, Oak Ridge, Tennessee, 1998.
- Lewis, K. M., Mitchell, B. G., van Dijken, G. L., and Arrigo, K. R.: Regional chlorophyll *a* algorithms in the Arctic Ocean and their effect on satellite-derived primary production estimates, *Deep-Sea Res. II*, 130, 17–24, <https://doi.org/10.1016/j.dsr2.2016.04.020>, 2016.
- Loose, B., McGillis, W. R., Schlosser, P., Perovich, D., and Takahashi, T.: Effects of freezing, growth, and ice cover on gas transport processes in laboratory seawater experiments, *Geophys. Res. Lett.*, 36, L05603, <https://doi.org/10.1029/2008GL036318>, 2009.
- Lueker, T. J., Dickson, A. G., and Keeling, C. D.: Ocean pCO<sub>2</sub> calculated from dissolved inorganic carbon, alkalinity, and equations for K<sub>1</sub> and K<sub>2</sub>: validation based on laboratory measurements of CO<sub>2</sub> in gas and seawater at equilibrium, *Mar. Chem.*, 70, 105–119, 2000.
- Manizza, M., Follows, M. J., Dutkiewicz, S., Menemenlis, D., McClelland, J. W., Hill, C. N., Peterson, B. J., and Key, R. M.: A model of the Arctic Ocean carbon cycle, *J. Geophys. Res.*, 116, C12020, <https://doi.org/10.1029/2011JC006998>, 2011.
- Maréchal, D.: A soil-based approach to rainfall-runoff modelling in ungauged catchments for England and Wales, PhD thesis, Cranfield University, UK, 157 pp., 2004.
- Maritorena, S., d'Andon, O. H. F., Mangin, A., and Siegel, D. A.: Merged satellite ocean color data products using a bio-optical model: Characteristics, benefits and issues, *Remote Sens. Environ.*, 114, 1791–1804, <https://doi.org/10.1016/j.rse.2010.04.002>, 2010.
- Matsuoka, A., Huot, Y., Shimada, K., Saitoh, S., and Babin, M.: Bio-optical characteristics of the western Arctic Ocean: Implications for ocean color algorithms, *Can. J. Remote Sens.*, 33, 503–518, <https://doi.org/10.5589/m07-059>, 2007.
- Meier, W., Fetterer, F., Savoie, M., Mallory, S., Duerr, R., and Stroeve, J.: NOAA/NSIDC Climate Data Record of Passive Microwave Sea Ice Concentration, Version 2, Boulder, Colorado USA, National Snow and Ice Data Center, <https://doi.org/10.7265/N55M63M1>, 2013.
- Moore, T. S., Dowell, M. D., and Franz, B. A.: Detection of coccolithophore blooms in ocean color satellite imagery: A generalized approach for use with multiple sensors, *Remote Sens. Environ.*, 117, 249–263, <https://doi.org/10.1016/j.rse.2011.10.001>, 2012.
- Mucci, A., Lansard, B., Miller, L. A., and Papakyriakou, T. N.: CO<sub>2</sub> fluxes across the air-sea interface in the southeastern Beaufort Sea: Ice-free period, *J. Geophys. Res.*, 115, C04003, <https://doi.org/10.1029/2009JC005330>, 2010.
- Murata, A.: Increased surface seawater pCO<sub>2</sub> in the eastern Bering Sea shelf: An effect of blooms of coccolithophorid *Emiliania huxleyi*?, *Global Biogeochem. Cycles*, 20, GB4006, <https://doi.org/10.1029/2005GB002615>, 2006.
- Murray, F. W.: On the computation of saturation vapor pressure, *J. Appl. Meteorol.*, 6, 203–204, 1967.
- Nakaoka, S., Telszewski, M., Nojiri, Y., Yasunaka, S., Miyazaki, C., Mukai, H., and Usui, N.: Estimating temporal and spatial variation of ocean surface pCO<sub>2</sub> in the North Pacific using a self-organizing map neural network technique, *Biogeosciences*, 10, 6093–6106, <https://doi.org/10.5194/bg-10-6093-2013>, 2013.
- Olsen, A., Brown, K. R., Chierici, M., Johannessen, T., and Neill, C.: Sea-surface CO<sub>2</sub> fugacity in the subpolar North Atlantic, *Biogeosciences*, 5, 535–547, <https://doi.org/10.5194/bg-5-535-2008>, 2008.
- Olsen, A., Key, R. M., van Heuven, S., Lauvset, S. K., Velo, A., Lin, X., Schirnick, C., Kozyr, A., Tanhua, T., Hoppema, M., Jutterström, S., Steinfeldt, R., Jeansson, E., Ishii, M., Pérez, F. F., and Suzuki, T.: The Global Ocean Data Analysis Project version 2 (GLODAPv2) – an internally consistent data product for the world ocean, *Earth Syst. Sci. Data*, 8, 297–323, <https://doi.org/10.5194/essd-8-297-2016>, 2016.
- O'Reilly, J. E., Maritorena, S., Mitchell, B. G., Siegel, D. A., Carder, K. L., Garver, S. A., Kahru, M., and McClain, C.: Ocean color chlorophyll algorithms for SeaWiFS, *J. Geophys. Res.*, 103, 24937–24953, <https://doi.org/10.1029/98JC02160>, 1998.
- Pabi, S., van Dijken, G. L., and Arrigo, K. R.: Primary production in the Arctic Ocean, 1998–2006, *J. Geophys. Res.*, 113, C08005, <https://doi.org/10.1029/2007JC004578>, 2008.
- Peng, G., Meier, W. N., Scott, D. J., and Savoie, M. H.: A long-term and reproducible passive microwave sea ice concentration data record for climate studies and monitoring, *Earth Syst. Sci. Data*, 5, 311–318, <https://doi.org/10.5194/essd-5-311-2013>, 2013.
- Perrette, M., Yool, A., Quartly, G. D., and Popova, E. E.: Near-ubiquity of ice-edge blooms in the Arctic, *Biogeosciences*, 8, 515–524, <https://doi.org/10.5194/bg-8-515-2011>, 2011.
- Popova, E. E., Yool, A., Coward, A. C., Dupont, F., Deal, C., Elliott, S., Hunke, E., Jin, M., Steele, M., and Zhang, J.: What controls primary production in the Arctic Ocean? Results from an intercomparison of five general circulation models with biogeochemistry, *J. Geophys. Res.*, 117, C00D12, <https://doi.org/10.1029/2011JC007112>, 2012.

- Reynolds, R. W., Rayner, N. A., Smith, T. M., Stokes, D. C., and Wang, W.: An improved in situ and satellite SST analysis for climate, *J. Climate*, 15, 1609–1625, 2002.
- Schuster, U., McKinley, G. A., Bates, N., Chevallier, F., Doney, S. C., Fay, A. R., González-Dávila, M., Gruber, N., Jones, S., Krijnen, J., Landschützer, P., Lefèvre, N., Manizza, M., Mathis, J., Metzl, N., Olsen, A., Rios, A. F., Rödenbeck, C., Santana-Casiano, J. M., Takahashi, T., Wanninkhof, R., and Watson, A. J.: An assessment of the Atlantic and Arctic sea–air CO<sub>2</sub> fluxes, 1990–2009, *Biogeosciences*, 10, 607–627, <https://doi.org/10.5194/bg-10-607-2013>, 2013.
- Semiletov, I., Makshtas, A., Akasofu, S.-I., and Andreas, E. L.: Atmospheric CO<sub>2</sub> balance: The role of Arctic sea ice, *Geophys. Res. Lett.*, 31, L05121, <https://doi.org/10.1029/2003GL017996>, 2004.
- Semiletov, I. P., Pipko, I. I., Repina, I., and Shakhova, N. E.: Carbonate chemistry dynamics and carbon dioxide fluxes across the atmosphere–ice–water interfaces in the Arctic Ocean: Pacific sector of the Arctic, *J. Mar. Syst.*, 66, 204–226, <https://doi.org/10.1016/j.jmarsys.2006.05.012>, 2007.
- Shutler, J. D., Land, P. E., Brown, C. W., Findlay, H. S., Donlon, C. J., Medland, M., Snooke, R., and Blackford, J. C.: Coccolithophore surface distributions in the North Atlantic and their modulation of the air–sea flux of CO<sub>2</sub> from 10 years of satellite Earth observation data, *Biogeosciences*, 10, 2699–2709, <https://doi.org/10.5194/bg-10-2699-2013>, 2013.
- Signorini, S. R. and McClain, C. R.: Effect of uncertainties in climatologic wind, ocean pCO<sub>2</sub>, and gas transfer algorithms on the estimate of global sea-air CO<sub>2</sub> flux, *Global Biogeochem. Cycles*, 23, GB2025, <https://doi.org/10.1029/2008GB003246>, 2009.
- Siswanto, E., Tang, J., Ahn, Y.-H., Ishizaka, J., Yoo, S., Kim, S.-W., Kiyomoto, Y., Yamada, K., Chiang, C., and Kawamura, H.: Empirical ocean color algorithms to retrieve chlorophyll *a*, total suspended matter, and colored dissolved organic matter absorption coefficient in the Yellow and East China Seas, *J. Oceanogr.*, 67, 627, <https://doi.org/10.1007/s10872-011-0062-z>, 2011.
- Siswanto, E., Ishizaka, J., Tripathy, S. C., and Miyamura, K.: Detection of harmful algal blooms of *Karenia mikimotoi* using MODIS measurements: a case study of Seto-Inland Sea, Japan, *Remote Sens. Environ.*, 129, 185–196, <https://doi.org/10.1016/j.rse.2012.11.003>, 2013.
- Smyth, T. J., Tyrrell, T., and Tarrant, B.: Time series of coccolithophore activity in the Barents Sea, from twenty years of satellite imagery, *Geophys. Res. Lett.*, 31, L11302, <https://doi.org/10.1029/2004GL019735>, 2004.
- Steele, M., Morley, R., and Ermold, W.: PHC: A global ocean hydrography with a high quality Arctic Ocean, *J. Climate*, 14, 2079–2087, 2001.
- Sweeney, C., Gloor, E., Jacobson, A. R., Key, R. M., McKinley, G., Sarmiento, J. L., and Wanninkhof, R.: Constraining global air–sea gas exchange for CO<sub>2</sub> with recent bomb <sup>14</sup>C measurements, *Global Biogeochem. Cycles*, 21, GB2015, <https://doi.org/10.1029/2006GB002784>, 2007.
- Takahashi, T., Sutherland, S. C., Wanninkhof, R., Sweeney, C., Feely, R. A., Chipman, D. W., Hales, B., Friederich, G., Chavez, F., Sabine, C., Watson, A., Bakker, D. C. E., Schuster, U., Metzl, N., Yoshikawa-Inoue, H., Ishii, M., Midorikawa, T., Nojiri, Y., Körtzinger, A., Steinhoff, T., Hoppema, M., Olafsson, J., Arnarson, T. S., Tilbrook, B., Johannessen, T., Olsen, A., Bellerby, R., Wong, C. S., Delille, B., Bates, N. R., and de Baar, H. J. W.: Climatological mean and decadal changes in surface ocean pCO<sub>2</sub>, and net sea–air CO<sub>2</sub> flux over the global oceans, *Deep-Sea Res. II*, 56, 554–577, 2009.
- Takahashi, T., Sutherland, S. C., and Kozyr, A.: Global Ocean Surface Water Partial Pressure of CO<sub>2</sub> Database: Measurements Performed During 1957–2014 (Version 2014). ORNL/CDIAC-160, NDP-088(V2014), Carbon Dioxide Information Analysis Center, Oak Ridge National Laboratory, U.S. Department of Energy, Oak Ridge, Tennessee, [https://doi.org/10.3334/CDIAC/OTG.NDP088\(V2014\)](https://doi.org/10.3334/CDIAC/OTG.NDP088(V2014)), 2015.
- Tassan, S.: Local algorithms using SeaWiFS data for the retrieval of phytoplankton, pigments, suspended sediment, and yellow substance in coastal waters, *Appl. Optics*, 33, 2369–2378, <https://doi.org/10.1364/AO.33.002369>, 1994.
- Telszewski, M., Chazottes, A., Schuster, U., Watson, A. J., Moulin, C., Bakker, D. C. E., González-Dávila, M., Johannessen, T., Körtzinger, A., Lüger, H., Olsen, A., Omar, A., Padin, X. A., Ríos, A. F., Steinhoff, T., Santana-Casiano, M., Wallace, D. W. R., and Wanninkhof, R.: Estimating the monthly pCO<sub>2</sub> distribution in the North Atlantic using a self-organizing neural network, *Biogeosciences*, 6, 1405–1421, <https://doi.org/10.5194/bg-6-1405-2009>, 2009.
- Ulfso, A., Cassar, N., Korhonen, M., van Heuven, S., Hoppema, M., Kattner, G., and Anderson, G. L.: Late summer net community production in the central Arctic Ocean using multiple approaches, *Global Biogeochem. Cycles*, 28, 1129–1148, <https://doi.org/10.1002/2014GB004833>, 2014.
- van Heuven, S., Pierrot, D., Lewis, E., and Wallace, D. W. R.: MATLAB Program Developed for CO<sub>2</sub> System Calculations, ORNL/CDIAC-105b. Carbon Dioxide Information Analysis Center, Oak Ridge National Laboratory, US Department of Energy, Oak Ridge, Tennessee, 2009.
- Wanninkhof, R.: Relationship between wind speed and gas exchange over the ocean, *J. Geophys. Res.*, 97, 7373–7382, <https://doi.org/10.1029/92JC00188>, 1992.
- Wanninkhof, R.: Relationship between wind speed and gas exchange over the ocean revisited, *Limnol. Oceanogr.-Methods*, 12, 351–362, 2014.
- Wanninkhof, R., Park, G.-H., Takahashi, T., Sweeney, C., Feely, R., Nojiri, Y., Gruber, N., Doney, S. C., McKinley, G. A., Lenton, A., Le Quéré, C., Heinze, C., Schwinger, J., Graven, H., and Khatiwala, S.: Global ocean carbon uptake: magnitude, variability and trends, *Biogeosciences*, 10, 1983–2000, <https://doi.org/10.5194/bg-10-1983-2013>, 2013.
- Weiss, R. F.: Carbon dioxide in water and seawater: the solubility of a non-ideal gas, *Mar. Chem.*, 2, 203–215, 1974.
- Yasunaka, S., Nojiri, Y., Nakaoka, S., Ono, T., Whitney, F. A., and Telszewski, M.: Mapping of sea surface nutrients in the North Pacific: Basin-wide distribution and seasonal to inter-annual variability, *J. Geophys. Res.-Oceans*, 119, 7756–7771, <https://doi.org/10.1002/2014JC010318>, 2014.
- Yasunaka, S., Murata, A., Watanabe, E., Chierici, M., Fransson, A., van Heuven, S., Hoppema, M., Ishii, M., Johannessen, T., Kosugi, N., Lauvset, S. K., Mathis, J. T., Nishino, S., Omar, A. M., Olsen, A., Sasano, D., Takahashi, T., and Wanninkhof, R.: Mapping of the air–sea CO<sub>2</sub> flux in the Arctic Ocean and its adjacent seas: basin-wide distribution and

seasonal to interannual variability, *Polar Sci.*, 10, 323–334, <https://doi.org/10.1016/j.polar.2016.03.006>, 2016.

Yasunaka, S.: CO<sub>2</sub> flux v.2, available at: <http://www.jamstec.go.jp/res/ress/yasunaka/co2flux/>, last access: 5 March 2018.

Zeng, J., Nojiri, Y., Landschützer, P., Telszewski, M., and Nakaoka, S.: A global surface ocean *f*CO<sub>2</sub> climatology based on a feed-forward neural network, *J. Atmos. Ocean Technol.*, 31, 1838–1849, <https://doi.org/10.1175/JTECH-D-13-00137.1>, 2014.